# A detailed quantitative analysis of sparse-Lagrangian filtered density function simulations in constant and variable density reacting jet flows

M. J. Cleary and A. Y. Klimenko

Citation: Phys. Fluids 23, 115102 (2011); doi: 10.1063/1.3657085
View online: http://dx.doi.org/10.1063/1.3657085
View Table of Contents: http://pof.aip.org/resource/1/PHFLE6/v23/i11
Published by the American Institute of Physics.

# A detailed quantitative analysis of sparse-Lagrangian filtered density function simulations in constant and variable density reacting jet flows

M. J. Cleary[a] and A. Y. Klimenko
*School of Mechanical and Mining Engineering, The University of Queensland, Queensland 4072, Australia*

(Received 30 May 2011; accepted 5 October 2011; published online 9 November 2011)

Sparse-Lagrangian filtered density function (FDF) simulations using a generalized multiple mapping conditioning mixing model and density coupling via a conditional form of the equivalent enthalpy method are performed for both constant density and variable density turbulent jet diffusion flames. The consistency between the sparse-Lagrangian FDF for the reactive species and the Eulerian large eddy simulation (LES) for velocity along with the accuracy of the reactive species predictions relative to the exact equilibrium solution are presented in detail. The sensitivity to the number of particles used in the simulations, the mixing localization structure, chemistry and numerical time step are all investigated. The analysis shows that consistency between the FDF and LES fields is relatively insensitive to the sparseness of the particle distributions and other model parameters but that the reactive species are strongly dependent on the degree of mixing localization in the LES mixture fraction space. An algorithm is developed to control the localization for any sparse distribution of particles with inter-particle distances within the inertial range, and it is shown that reactive species predictions are sensitive to the mixing distance in a reference mixture fraction space while there is very low sensitivity to the number of particles used in the simulations. © *2011 American Institute of Physics*. [doi:10.1063/1.3657085]

## I. INTRODUCTION

The advance of computing power has increasingly made large eddy simulation (LES) a viable approach for modeling turbulent reacting flows. In its most common combustion modeling form, LES involves a spatial filtering operation whereby the large scale motions are resolved and the small dissipative scale eddies are modeled. Since chemical reaction rates in turbulent flows are strongly affected by the turbulence-chemistry interactions at the unresolved scales, the filtered chemical source term in the LES reactive scalar transport equation cannot be closed solely from the resolved scale information. The concept of the filtered density function (FDF), defined as the probability density function (PDF) of subfilter fluctuations,[1] was developed to permit a probabilistic treatment of the LES subfilter scale. Gao and O'Brien,[2] and later Colucci *et al.*,[3] derive the joint scalar FDF transport equation and illustrate the great advantage associated with such methods—the FDF chemical reaction rate appears in closed form thus alleviating the primary closure problem identified above. A series of papers have since systematically advanced the FDF method to establish the governing equations and convergence of Monte Carlo numerical schemes for the joint scalar filtered mass-weighted density function (FMDF) for variable density flows,[4] the velocity FDF,[5] the joint velocity-scalar FDF,[6] and the joint velocity-scalar FMDF.[7] For the remainder of this paper, the term FDF is used generally to describe FDF and FMDF methods. Unless otherwise noted closure is assumed to be at the joint scalar level whereby reactive scalars are simulated by the FDF and the velocity is simulated by conventional Eulerian LES. Validation of FDF methods against experimental data was first performed by Zhou and Pereira[8] for a 2D isothermal mixing layer. Validation against inhomogeneous jet flame experimental data using tabulated chemical source closure is found in Sheikhi *et al.*[9] and Raman *et al.*[10] and the first fully closed FDF simulation with detailed 16-step chemistry was performed by Raman and Pitsch.[11] Drozda *et al.*[12] provide a comprehensive review of FDF developments and applications, and in a general review of PDF methods, Haworth[13] includes an extensive discussion on the FDF subset. FDF methods also feature in the combustion LES review by Pitsch.[14]

The FDF transport equations are derived from the Eulerian perspective, but to minimize computational cost, the FDF is conventionally represented by an ensemble of Pope particles (Lagrangian particles with properties and a mixing operator over these properties[15]) observing a set of statistically equivalent stochastic Ito equations. A survey of published FDF applications[9–11] indicates that between 15 and 50 Pope particles are typically employed per Eulerian grid-cell used for the LES of the velocity field. Such *intensive-Lagrangian* FDF simulations can involve 10s or 100s of millions of Pope particles across a laboratory-scale flow domain. Although the predictions are very good, the computational cost is high. Therefore, an extension of intensive-Lagrangian FDF methods to practical, engineering-scale combustion systems with realistic chemical kinetics is enormously costly given current computing power.[14] However, the FDF can in fact be modeled with relatively few Pope particles and therefore at very low cost using a *sparse-Lagrangian* FDF implementation. The term *sparse-Lagrangian* is used to denote simulations where there are significantly fewer Pope particles for the reactive scalar field than there are Eulerian grid-cells in the LES of

[a]Author to whom correspondence should be addressed. Electronic mail: m.cleary@uq.edu.au. Tel.: +61-7-3365 4069. Fax: +61-7-3365 4799.

 

velocity. The feasibility of sparse-Lagrangian simulations using as few as 10 000 reacting Pope particles has been demonstrated for Sandia Flames D and E.[16–18] Due to the very low cost (up to 3 orders of magnitude lower than intensive simulations), the sparse computations were possible for detailed 219-step chemistry and were performed on a single personal workstation. First and second unconditional and conditional moments of the reactive species are of comparable accuracy to previously published intensive-Lagrangian FDF simulations.

In addition to the practical demonstration of sparse methods,[16–18] their theory has been developed in a series of papers establishing convergence to direct numerical simulation (DNS) (Refs. 19 and 20) and LES (Refs. 21 and 15). Additionally, an intuitive, physical explanation of sparse methods is found in Ref. 17. Two fundamental modeling issues have been identified for accurate and consistent FDF simulation using a sparse distribution of Pope particles. The first of these is density coupling; the filtered mean density must be calculated from the relatively few particles and a value assigned to each of the more numerous LES grid-cells. A conditional equivalent enthalpy method was developed recently to address this situation.[18] While the original equivalent enthalpy method, developed by Muradoglu *et al.*[22] and demonstrated for intensive FDF simulations by Raman and Pitch,[11] ensures full consistency of FDF and LES treatments of density, the adapted conditional method[18] neglects the conditional fluctuations of the density.

The second modeling issue for accurate and consistent sparse FDF simulations relates to the localness of the mixing model which emulates the conditional subfilter scalar dissipation. As real fluid mixing takes place locally in physical space, this should be reflected in the simulations. Enforcement of sufficient physical localness of Pope particles to accurately mimic real fluid mixing is impractical, especially for sparse simulations, but mixing models which enforce localness in composition space have been found to work very well in the RANS/PDF context.[23] The model developed for sparse-Lagrangian FDF simulations is a generalized version[17] of the multiple mapping conditioning (MMC) framework for turbulent reactive flows.[24,25] In MMC, the mixing is localized within a reference space which is mathematically independent of the reactive composition field. This independence is highly desirable in a mixing model as it ensures that all chemical species mix equally and linearly.[13,23,26] The MMC reference space concept has much in common with the concepts developed in the intrinsic low dimensional manifold (ILDM)[27] and reaction-diffusion manifold (REDIM)[28] methods. At the same time, MMC incorporates conditional averaging and thus unifies joint PDF/FDF and conditional moment closure (CMC)[29] methodologies. For the sparse simulations of Flames D and E,[16,18] the MMC reference space is selected to be the filtered mixture fraction simulated by the Eulerian LES. This selection is based on the well known phenomenon that fluctuations of reactive scalars in turbulent diffusion flames correlate strongly with fluctuations of the mixture fraction and, as a result, localness in mixture fraction space implies a strong degree of localness in the reactive composition space.

There is also a principle numerical requirement of sparse-Lagrangian FDF simulations. Even though the FDF can be modelled accurately and consistently with sparse-Lagrangian methods observation of the instantaneous and local moments of the FDF such as the filtered mean or subfilter variance requires a large number of Pope particles else stochastic error is large. It is possible to evaluate stationary statistics with those relatively few remaining particles by accumulation in time, or alternatively the observation length scale can be increased to encompass a greater number of particles for evaluation of instantaneous but less local statistics. These two alternative approaches to observing the reactive scalar statistics correspond to complementary perspectives of the model. The first is the MMC perspective—the model is a PDF model based on conditioning in a reference space and the Eulerian LES is simply an input that provides the simulated reference variables. The second is the LES perspective—the model is an FDF model for the LES subgrid although the fine grain statistics are not instantaneously observable at that scale.

In this paper, we present a detailed quantitative analysis of sparse-Lagrangian FDF simulations with a generalized MMC closure. While previous publications have theoretically developed the model and computationally demonstrated its potential against laboratory flame data, here we perform a thorough quantitative assessment of the model and its numerical implementation for idealized jet flame conditions. The flame is a simple jet and chemical reactions occur in a thin reaction zone near the stoichiometric contour. Both constant and variable density flows are investigated. The structure of the paper is as follows. Section II presents the transport equations for the LES and the joint-scalar FDF. The generalized MMC mixing model closure is developed in detail in Sec. III and Sec. IV describes the conditional equivalent enthalpy method for density coupling. Section V presents a description of the simulated test cases and the numerical and modeling parameters that are used. Results appear in Sec. VI which contains analysis of the localization parameters, a demonstration of consistency between the LES and FDF fields for a number of sparse-Lagrangian particle distributions, and analysis of reactive scalar predictions including sensitivity to various model and numerical parameters. Finally Sec. VII contains discussion and conclusions.

## II. LES AND FDF FORMULATIONS

A hybrid Eulerian/Lagrangian method is used, consisting of an Eulerian LES for the simulation of velocity, pressure, and reference mixture fraction and a Lagrangian formulation of the FDF for the simulation of the reactive composition field. In this section, the two schemes are presented independently while a description of the density coupling method is left until Sec. IV. Complete derivations of the LES and FDF transport equations are found elsewhere[3,4,30] and here we present only the main equations and closures.

### A. The large eddy simulation

In its most conventional form LES involves a spatial filtering operation. The filtered or resolved quantity is given by

$$\bar{\varphi}(x,t) = \int_{-\infty}^{\infty} \varphi(x',t)G(x'-x)dx', \tag{1}$$

where $\varphi$ is the unfiltered quantity and $G$ is a kernel function of width $\Delta_E$ which satisfies the requirement that

$$\bar{\rho}(x,t) = \int_{-\infty}^{\infty} \rho(x',t)G(x'-x)dx'. \tag{2}$$

In variable density flows, a density-weighted filter is applied giving the Favre filtered quantity

$$\tilde{\varphi} = \frac{\overline{\rho\varphi}}{\bar{\rho}}. \tag{3}$$

Application of the Favre filter to the conservation equations for mass, momentum, and reference mixture fraction gives

$$\frac{\partial\bar{\rho}}{\partial t} + \frac{\partial\bar{\rho}\tilde{u}_i}{\partial x_i} = 0, \tag{4}$$

$$\frac{\partial\bar{\rho}\tilde{u}_j}{\partial t} + \frac{\partial\bar{\rho}\tilde{u}_i\tilde{u}_j}{\partial x_i} = -\frac{\partial\bar{P}}{\partial x_j} + \frac{\partial}{\partial x_i}\left(\tilde{\tau}_{ij} - \tau_{ij}^{\mathrm{sf}}\right), \tag{5}$$

$$\frac{\partial\bar{\rho}\tilde{f}}{\partial t} + \frac{\partial\bar{\rho}\tilde{u}_i\tilde{f}}{\partial x_i} = -\frac{\partial}{\partial x_i}\left(\tilde{J}_{f,i} + J_{f,i}^{\mathrm{sf}}\right). \tag{6}$$

Here, $\tilde{\tau}_{ij}$ and $\tilde{J}_{f,i}$ are the resolved viscous stress tensor and resolved diffusive flux, respectively,

$$\tilde{\tau}_{ij} = \bar{\rho}\nu\left(\frac{\partial\tilde{u}_i}{\partial x_j} + \frac{\partial\tilde{u}_j}{\partial x_i} - \frac{2}{3}\frac{\partial\tilde{u}_k}{\partial x_k}\delta_{ij}\right) = \bar{\rho}\nu\left(2\tilde{S}_{ij} - \frac{2}{3}\tilde{\tau}_{kk}\delta_{ij}\right), \tag{7}$$

$$\tilde{J}_{f,i} = -\bar{\rho}\mathscr{D}\frac{\partial\tilde{f}}{\partial x_i}. \tag{8}$$

In the above $\nu$ is the kinematic viscosity and, in the present work, the molecular diffusivity is given by $\mathscr{D} = \nu/\sigma$ where $\sigma = 0.7$ is the Schmidt number.

The filtered equations contain a number of unclosed terms which are now briefly discussed. Development of closure models for the subfilter stress $\tau_{ij}^{\mathrm{sf}} = \bar{\rho}\left(\widetilde{u_iu_j} - \tilde{u}_i\tilde{u}_j\right)$ is ongoing; some of the major methods are critically evaluated by Meneveau and Katz.[31] In common with other combustion LES publications,[10,11,32,33] we adopt the relatively simple eddy viscosity model

$$\tau_{ij}^{\mathrm{sf}} - \frac{\delta_{ij}}{3}\tau_{kk}^{\mathrm{sf}} = -\bar{\rho}\nu_t\left(2\tilde{S}_{ij} - \frac{2}{3}\tilde{\tau}_{kk}\delta_{ij}\right), \tag{9}$$

with a Smagorinsky closure for $\nu_t$ (Ref. 34)

$$\nu_t = C_s\Delta_E^2\sqrt{2\tilde{S}_{ij}\tilde{S}_{ij}}, \tag{10}$$

where the coefficient $C_s$ is determined dynamically.[35] The purpose of the additional term $-\delta_{ij}/3\tau_{kk}^{\mathrm{sf}}$ on the lhs of Eq. (9) is to avoid a trace-free subfilter stress tensor and it is compensated for in the pressure term in the filtered momentum equation. The subfilter mass fluxes $J_{f,i}^{\mathrm{sf}} = \bar{\rho}\left(\widetilde{u_if} - \tilde{u}_i\tilde{f}\right)$ in Eq. (6) are determined according to an eddy diffusivity model

$$J_{f,i}^{\mathrm{sf}} = -\bar{\rho}\mathscr{D}_t\frac{\partial\tilde{f}}{\partial x_i}, \tag{11}$$

where $\mathscr{D}_t = \nu_t/\sigma_t$ and $\sigma_t = 1$ is the turbulent Schmidt number.

### B. The filtered density function

For the composition scalar field, $\phi = (\phi_1, \ldots, \phi_\alpha, \ldots, \phi_{ns})$, the subfilter turbulent fluctuations are represented probabilistically by the filtered mass density function, $F_L$, defined as

$$F_L(\boldsymbol{\psi};x,t) = \int_{-\infty}^{+\infty} \rho(x',t)\zeta[\boldsymbol{\psi},\boldsymbol{\phi}(x',t)]G(x'-x)dx', \tag{12}$$

where $\boldsymbol{\psi}$ is the sample space for $\boldsymbol{\phi}$ and the fine-grained density, $\zeta$, is given by the $n_s$-dimensional delta function

$$\zeta[\boldsymbol{\psi},\boldsymbol{\phi}(x,t)] = \delta[\boldsymbol{\psi} - \boldsymbol{\phi}(x,t)] = \prod_{\alpha=1}^{n_s}\delta[\psi_\alpha - \phi_\alpha(x,t)]. \tag{13}$$

From Eqs. (2) and (12), it is apparent that integration of the generalized function $F_L$ in scalar space yields the filtered density

$$\int_{-\infty}^{+\infty} F_L(\boldsymbol{\psi};x,t)d\boldsymbol{\psi} = \bar{\rho}(x,t). \tag{14}$$

Furthermore, defining the conditional Favre filtered mean of some variable $\phi$ as

$$\overline{\varphi(x,t)|\boldsymbol{\psi}} = \frac{\int_{-\infty}^{+\infty}\rho(x',t)\varphi(x',t)\zeta[\boldsymbol{\psi},\boldsymbol{\phi}(x',t)]G(x'-x)dx'}{F_L(\boldsymbol{\psi};x,t)}, \tag{15}$$

its (unconditional) filtered mean is therefore given by

$$\tilde{\varphi}(x,t) = \frac{1}{\bar{\rho}}\int_{-\infty}^{+\infty}\overline{\varphi(x,t)|\boldsymbol{\psi}}F_L(\boldsymbol{\psi};x,t)d\boldsymbol{\psi}. \tag{16}$$

The exact transport equation for the temporal and spatial evolution of $F_L$ as derived by Jaberi *et al.*[4] is

$$\frac{\partial F_L}{\partial t} + \frac{\partial\overline{u_i|\boldsymbol{\psi}}F_L}{\partial x_i} = \frac{\partial}{\partial\psi_\alpha}\left(\overline{\frac{1}{\rho(\boldsymbol{\psi})}\frac{\partial J_{\alpha,i}}{\partial x_i}|\boldsymbol{\psi}}F_L\right) - \frac{\partial W_\alpha(\boldsymbol{\psi})F_L}{\partial\psi_\alpha}. \tag{17}$$

Note that the chemical reaction rate, $W_\alpha$, appears in closed form whereas the conditional convective flux and conditional diffusive flux terms are both unclosed and require modeling. By decomposing the conditional velocity as

$$\overline{u_i|\boldsymbol{\psi}}F_L = \tilde{u}_i F_L + \left(\overline{u_i|\boldsymbol{\psi}} - \tilde{u}_i\right)F_L, \tag{18}$$

its closure can then be obtained through use of gradient model for the second term on the rhs of Eq. (18)[3]

$$\left(\overline{u_i|\boldsymbol{\psi}} - \tilde{u}_i\right)F_L = -\bar{\rho}\mathscr{D}_t \frac{\partial F_L/\bar{\rho}}{\partial x_i}. \tag{19}$$

Similarly, decomposing the conditional diffusive flux term on the rhs of Eq. (17) into resolved and subfilter parts and substituting a gradient diffusion flux model similar to Eq. (8) gives

$$\frac{\partial}{\partial \psi_\alpha}\left(\overline{\frac{1}{\rho(\boldsymbol{\psi})}\frac{\partial J_{\alpha,i}}{\partial x_i}|\boldsymbol{\psi}}F_L\right) = \frac{\partial}{\partial x_i}\left(\bar{\rho}\mathscr{D}\frac{\partial F_L/\bar{\rho}}{\partial x_i}\right) - \frac{\partial^2}{\partial\psi_\alpha\partial\psi_\beta} \times \left[\overline{\bar{\rho}\mathscr{D}\frac{\partial\phi_\alpha}{\partial x_i}\frac{\partial\phi_\beta}{\partial x_i}|\boldsymbol{\psi}}F_L/\bar{\rho}\right], \tag{20}$$

where to ensure consistency with the LES filtered scalar transport equation it has been assumed that[4]

$$\frac{\partial}{\partial x_i}\left(\bar{\rho}\mathscr{D}\frac{\partial F_L/\rho(\phi)}{\partial x_i}\right) = \frac{\partial}{\partial x_i}\left(\bar{\rho}\mathscr{D}\frac{\partial F_L/\bar{\rho}}{\partial x_i}\right). \tag{21}$$

The first term on the rhs of Eq. (20) accounts for the resolved-scale diffusive flux and the second term is the still unclosed subfilter conditional scalar dissipation. Its closure is discussed below in the context of the stochastic Lagrangian formulation of the FDF. With the above closures, the modeled FDF transport equation is

$$\frac{\partial F_L}{\partial t} + \frac{\partial}{\partial x_i}\left(\tilde{u}_i F_L - \bar{\rho}(\mathscr{D}+\mathscr{D}_t)\frac{\partial F_L/\bar{\rho}}{\partial x_i}\right) + \frac{\partial W_\alpha(\boldsymbol{\psi})F_L}{\partial\psi_\alpha} = -\frac{\partial^2}{\partial\psi_\alpha\partial\psi_\beta}\left(\overline{\bar{\rho}\mathscr{D}\frac{\partial\phi_\alpha}{\partial x_i}\frac{\partial\phi_\beta}{\partial x_i}|\boldsymbol{\psi}}F_L/\bar{\rho}\right). \tag{22}$$

The terms on the lhs of Eq. (22) are closed but the conditional subfilter scalar dissipation term on the rhs is still unclosed.

The FDF transport equation is $(n_s+3)$-dimensional where $n_s \gg 1$ for any realistic treatment of the chemical kinetics. To avoid the intractable cost of computing the density function via a finite-difference scheme whose cost increases exponentially with the number of dimensions, it is common practice to use a Lagrangian particle scheme for which cost increases approximately linearly with the number of dimensions. Therefore, Eq. (22) is replaced by the following equivalent stochastic differential equations:

$$dx_i^p = A_i^p dt + b_{ij}^p d\omega_j, \tag{23}$$

$$d\phi_\alpha^p = \left(W_\alpha^p + S_\alpha^p\right)dt. \tag{24}$$

Here, the superscript $p=1, 2, \ldots, N$ is a particle index and indicates a stochastic value evaluated on or assigned to the Pope particles. We use the shorthand notation $(\cdot)^p = (\cdot)(\boldsymbol{x}^p, t)$. $A_i$ and $b_{ij}$ are the drift and diffusion coefficients and $\omega_j$ is the independent Weiner process. Models for $A_i$ and $b_{i,j}$ are determined by comparison of the Fokker-Planck equation corresponding to Eq. (23) with the convection terms in the FDF transport equation.[3,4] Alternatively, they may be determined by considering the filtered continuous scalar transport as a Fokker-Planck equation for Lagrangian particle number density.[19] By either approach, we get

$$A_i = \tilde{u}_i + \frac{1}{\bar{\rho}}\frac{\partial}{\partial x_i}(\bar{\rho}(\mathscr{D}+\mathscr{D}_t)), \tag{25}$$

$$b_{ij} = \delta_{ij}\sqrt{2(\mathscr{D}+\mathscr{D}_t)}. \tag{26}$$

In Eq. (24), $S_\alpha$ is the unclosed mixing operator which emulates the conditional subfilter scalar dissipation on the rhs of Eq. (22). Various mixing models are available and may involve various forms of direct exchanges between Pope particles or interactions with filtered (or mean) values. The mixing models which are commonly used for PDF modeling are Curls[36] and modified Curls[37] models, interaction by exchange with the mean (IEM)[38] and the Euclidean minimum spanning tree (EMST) model.[23] The individual and relative performances of these models are extensively reviewed in the literature.[13,26] Other advanced mixing models are also under investigation.[39–42] Published FDF simulations mostly use the IEM mixing model. While IEM is very simple to implement, it has two deficiencies. First, the model preserves the shape of the subfilter distributions so that they are determined solely by initial and/or boundary conditions. Second, the IEM model does not ensure localness of mixing. In practical, intensive-Lagrangian FDF contexts these deficiencies are somewhat overcome due to the relatively smaller influence of the subfilter scale mixing on the macroscale features of the flow and the implicit localness resulting from the use of a well resolved grid. In sparse-Lagrangian FDF simulations, the inter-particle distance is relatively large and, as is the case for RANS/PDF modeling, the reactive scalar distributions can be very sensitive to the form of the mixing model. In the present work, mixing particles interact directly with each other, similarly to Curl's model, but the particle pairs are selected specifically rather than randomly so as to enforce localness in a reference space. The specific details of the particle pair selection by generalized MMC are discussed in Sec. III. Once selected, the pair of mixing particles, $p$ and $q$, mix linearly and discretely over a finite time step $\Delta t$ such that

$$\begin{aligned}\phi_\alpha^p(t+\Delta t) &= \phi_\alpha^p(t) + \mu\left(\bar{\phi}_\alpha^{p,q}(t) - \phi_\alpha^p(t)\right),\\ \phi_\alpha^q(t+\Delta t) &= \phi_\alpha^q(t) + \mu\left(\bar{\phi}_\alpha^{p,q}(t) - \phi_\alpha^q(t)\right),\end{aligned} \tag{27}$$

where $\bar{\phi}_\alpha^{p,q}$ is the two-particle mean, which may be weighted if variable mass particles are used, and $\mu = 1 - \exp(-\Delta t/\tau_L^{p,q})$ is the extent of mixing controlled by a mixing time scale, $\tau_L^{p,q}$. The mixing timescale is determined locally and instantaneously for each mixing pair and is related to the dissipation time. The selection of particle pairs and the associated model for $\tau_L$ are discussed in Sec. III.

## III. GENERALIZED MMC MIXING FOR SPARSE-LAGRANGIAN FDF SIMULATIONS

To this point, the model has been presented as a conventional FDF method which could be applied at high cost using a traditional intensive-Lagrangian particle scheme. Now, we depart from the conventional approach. In this section, a generalized MMC mixing model closure is developed which permits a very low cost sparse-Lagrangian implementation of the FDF method.

As described elsewhere,[25] MMC is a modeling framework based on a mapping to a set of reference variables. From that framework, specific models are formulated for specific combustion cases. Therefore, we briefly introduce the combustion case before describing the model closure. The flame chemistry is as described by Norris and Pope[43] and later used by Subramaniam and Pope[23] to test the localization ability of the EMST mixing model. The thermochemical state is represented by two variables: the mixture fraction, $Z$, and a single progress variable $Y$, whose equilibrium concentration, $Y^{eq}$, is a unique function of $Z$. The product is formed by an infinitely fast, one-step, irreversible reaction in a narrow stoichiometric region $R$ as shown in Fig. 1. Fuel and air mix turbulently towards the thin reaction zone and upon entering it are instantaneously converted to the equilibrium product composition.

The thinness of the reaction zone for this idealized flamesheet represents a particularly difficult test case for a mixing model. Upon mixing, the Pope particle compositions will depart from the equilibrium composition unless the as-mixed particle compositions fall within the thin reaction zone. To ensure that non-physical departures are avoided particle mixing pairs in the vicinity of stoichiometry should be local to each other by ensuring that $d_Z^{p,q} < \epsilon$ where $d_{(\cdot)}^{p,q} = |(\cdot)^p - (\cdot)^q|$ and $\epsilon$ is small number determined by the details of the flame chemistry. In the current example, we can see that the simulated composition will be unconditionally correct only if $d_Z^{p,q}$ is less than half the width of the reaction zone. The EMST mixing model enforces this localness condition directly by comparing $Z^p$ values of each particle in the ensemble and as such performs very well for the thin reaction zone conditions investigated here.[23] An alternative localization is used in MMC where mixing is local in a reference space which is mathematically independent of the instantaneous values of $(Z^p, Y^p)$. This ensures that MMC, unlike EMST, treats all scalars equally and linearly. The interpretation of independence that we use is that the reference and reactive composition fields must be modeled by different processes or equations. Of course some quantities within those independent equations, such as density and velocity, will be the same. Here, the reference space is given by the Eulerian filtered mixture fraction, $\tilde{f}$. By using the filtered field as the reference variable, the fine scale turbulent features are, by necessity, ignored in the localization. However, typically the distance between mixing particles is relatively large compared to the filter width applied to the reference variable and then use of the filtered quantity, $\tilde{f}$, is a justifiable and practical approach. The model now contains two simulated mixture fraction variables: $Z$ and $\tilde{f}$. The former, modeled stochastically according to Eqs. (23) and (24), is treated as a real mixture fraction for the purposes of evaluating the reactive scalar field, while the later, modeled according to Eq. (6), assists the simulation of the FDF by determining which particles are formed into pairs for mixing. MMC models can also have additional reference variables representing velocity, scalar dissipation, sensible enthalpy, or other useful quantities.[44–46] Since $Z$ and $\tilde{f}$ are independent of each other MMC does not strictly enforce localness in $(Z, Y)$ space. Therefore, it is important that the $Z$ and $\tilde{f}$ be topologically similar else localness in $\tilde{f}$ would not reliably imply localness in $Z$.

Particle mixing pairs are selected so that their separation in $\tilde{f}$-space is less than some scale whose characteristic value is denoted by $f_m$. Once that criterion is satisfied, their separating distance in physical space should also be as small as possible. The characteristic physical separation scale is denoted as $r_m$. The correspondence between the scales $f_m$ and $r_m$ can be approximated by considering isoscalar contours in a turbulent field. Fig. 2 shows a segment of an isoscalar sliver

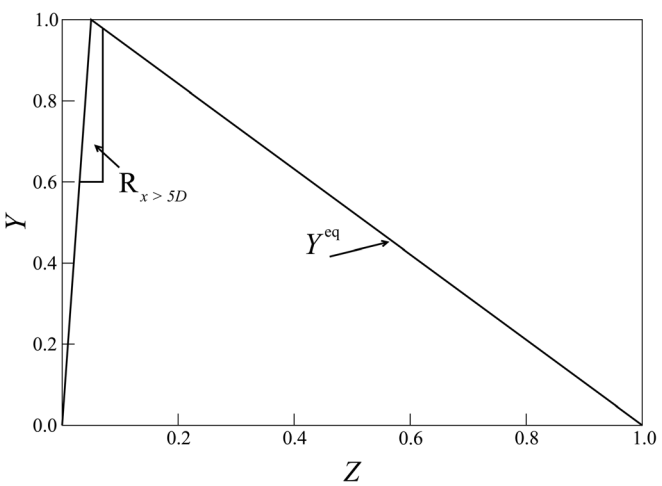


FIG. 1. Sketch of the flamesheet chemistry showing the thin reaction zone $R$ where the progress variable instantaneously reaches its equilibrium value, $Y^{eq}$. Outside $R$ reactions do not occur.

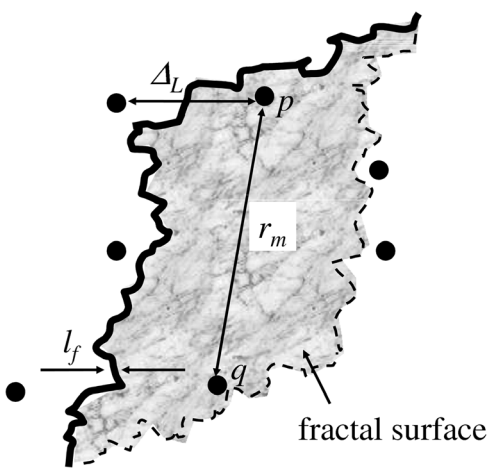


FIG. 2. Schematic of a mixing particle pair, $p$ and $q$, located on an isoscalar sliver of thickness $l_f$. The physical length scale between mixing particles is $r_m$ while the length scale to the nearest particle is $\Delta_L$. The scalar surface is modeled as a fractal of dimension $D_f = 2.36$ and with inner cutoff scale $r_c$.

which has a thickness $l_f \sim f_m/\left(d\tilde{f}/dn\right)$, where $d\tilde{f}/dn$ is the gradient normal to the isoscalar sliver. A particle mixing pair, $p$ and $q$, is selected such that they are the physically closest particles with the condition that they are both located within the isoscalar sliver. Assuming that the surface of the sliver has fractal properties, its area is $A_f \sim (r_c/r_m)^{2-D_f} r_m^2$, where $r_c$ is the inner cutoff scale and $D_f$ is the fractal dimension. Fractal properties in turbulence are discussed in a number of publications.[47,48] It seems that the experimentally observed fractal dimension is 2.36.[48] In the LES, the inner cutoff scale is the filter width: $r_c = \Delta_E$. In Monte Carlo simulations, the number of particles found within a certain volume is independent of the shape of that volume and so the particle mixing volume $V_m \sim l_f A_f$ is equal to the volume of fluid that is represented by each particle $V_p \sim \Delta_L^3$. Here, the nominal distance between particles, $\Delta_L$, is the mean distance between nearest particles in physical space without any consideration as to which particles actually form mixing pairs. Thus, $\Delta_L$ is an input parameter determined by the number of particles used in the simulations. Equating $V_m$ and $V_p$ we get

$$r_m = C_m \left( \frac{d\tilde{f}}{dn} \frac{\Delta_L^3}{r_c^{2-D_f}} \frac{1}{f_m} \right)^{1/D_f}, \tag{28}$$

where $C_m$ is a constant determined by matching $r_m$ to the actual mixing distance, $d_x^{p,q}$, observed in the simulations; we find $C_m = 0.5$ works well. In the results, it is shown that two sparse simulations with different $\Delta_L$ can yield the same reactive scalar predictions by keeping $f_m$ the same. From the above scaling, we get $r_{m1}/r_{m2} = (\Delta_{L2}/\Delta_{L1})^{3/D_f}$ where subscripts 1 and 2 denote two simulations with different sparse distributions of particles.

Selection of particle pairs to satisfy the above criteria is achieved by minimizing the effective square distance between particles defined as[16,18]

$$\hat{d}_{p,q}^2 = \sum_{i=1}^{3} \left( \frac{d_{x_i}^{p,q}}{r_i} \right)^2 + \left( \frac{d_{\tilde{f}}^{p,q}}{f_m} \right)^2, \tag{29}$$

where $r_i$ is the characteristic mixing distance in each spatial direction. Although selecting different physical scales in different directions could be of benefit, we keep the model simple and set $r_i = r_m/\sqrt{3}$ for $i = 1$, 2, and 3, where the $\sqrt{3}$ denominator is based on the assumption that particle mixing distance is isotropic. Minimization of $\hat{d}_{p,q}^2$ leads to equality of the normalized distances $d_{x_i}^{p,q}/r_i$ and $d_{\tilde{f}}^{p,q}/f_m$. In fact, an approximate minimization method is used which is based on the k-d tree[49] as described in Ref. 16. We select $f_m$ as a global parameter. In general, $r_m$ is a local quantity which varies due to variations in $\Delta_L$ and $d\tilde{f}/dn$ according to Eq. (28). Having different $r_m$ at different locations in the flow would impose a large computational cost on the particle mixing pair selection algorithm and so we instead treat $r_m$ (like $f_m$) as a global parameter which is calculated using values of $\Delta_L$ and $d\tilde{f}/dn$ at a characteristic location in the flow. Here that location is the shear layer at the nozzle exit where the scalar gradient is at its largest. Consequently $d_{\tilde{f}}^{p,q}$ and $d_{\boldsymbol{x}}^{p,q}$ at all other locations will on average be less than or equal to $f_m$ and $r_m$, respectively. The structure of this localization scheme is analysed in detail in Sec. VI.

In previous publications,[16–18] mixing localness has been controlled by a parameter $\lambda$ which can be shown to be proportional to ratio $r_m/f_m$. The current notation has been adopted as it gives greater physical transparency to the mixing localization parameters.

We now present the model for the mixing time scale, $\tau_L^{p,q}$, which controls the extent of mixing, $\mu$, in Eq. (27) and thus determines the level of sub-Lagrangian-filter fluctuations (i.e., the fluctuations at the scale $d_{\boldsymbol{x}}^{p,q}$). Unless retained for emphasis, the particle index superscripts $p$ and $q$ are dropped here and in the remainder of the paper. It is understood that the parameters in the following expressions are associated with the particle locations (e.g., $d_{\boldsymbol{x}} \equiv d_{\boldsymbol{x}}^{p,q}$ is the physical distance between mixing particles and $\nabla\tilde{f} \equiv \left(\nabla\tilde{f}\right)^p$ is the gradient of the reference mixture fraction which is simulated in the LES and interpolated to the location of the particle). In sparse simulations $d_{\boldsymbol{x}}$ is not small and mixing will generate numerical diffusion proportional to $d_{\boldsymbol{x}}^2/\tau_L$.[19] For a given particle spacing $\tau_L$ must be selected to avoid excessive numerical diffusion. The value of $\tau_L$ can be determined by scale similarity between the FDF and LES fields in the inertial range as described in Ref. 18. The characteristic LES length is the Eulerian filter width, $\Delta_E$, with an associated characteristic Eulerian time scale, $\tau_E$. From the definition of the dissipation time scale as the ratio of subfilter scalar variance and scalar dissipation, we can write $\tau_E = \widetilde{f_E''^2}/\chi$ where $\widetilde{f_E''^2}$ is the subfilter variance of $\tilde{f}$ at the scale $\Delta_E$, and $\chi$ is the instantaneous scalar dissipation. Similarly, we define $\tau_L = \widetilde{f_L''^2}/\chi$. Assuming $\Delta_E$ and $d_{\boldsymbol{x}}$ are within the inertial range for which $\chi$ is universal, it follows that

$$\tau_L = C_L^{-1} \frac{\widetilde{f_L''^2}}{\widetilde{f_E''^2}} \tau_E. \tag{30}$$

Nominally $C_L = 1$. It was demonstrated previously[16] that $C_L$ can be tuned to effectively control the conditional variance of the reactive species. However, since that method involves scaling of the relation between the Lagrangian and Eulerian time scales it may also upset the consistency of the FDF and LES fields. In the present work, we set $C_L = 1$ and show that varying the mixing distance in $\tilde{f}$-space, through the explicit mixing parameter $f_m$, is an alternative and effective way of controlling conditional variance while still ensuring consistency between the FDF and LES fields.

Algebraic models are used for $\widetilde{f_E''^2}$, $\chi$, and $\widetilde{f_L''^2}$. For $\widetilde{f_E''^2}$ and $\chi$, the conventional combustion LES models[32] are used,

$$\widetilde{f_E''^2} = C_f \Delta_E^2 \nabla\tilde{f} \cdot \nabla\tilde{f} \tag{31}$$

and

$$\chi = 2(\mathscr{D} + \mathscr{D}_t) \nabla\tilde{f} \cdot \nabla\tilde{f}, \tag{32}$$

where $C_f = 0.1$. The quantity $\widetilde{f_L''^2}$ is particular to our sparse FDF simulations. Similar to the form of $\widetilde{f_E''^2}$ in Eq. (31), we model it as

$$\widetilde{f_L'^2} = C_f d_x^2 \beta \left(\frac{d_{\tilde{f}}}{d_x}\right)^2. \tag{33}$$

The coefficient $\beta$ is a number between 1 and 3; the latter value being for isotropic regions of the flow where the gradient is equal in all directions. Values of $\beta$ less than three imply anisotropy and result in smaller values of $\tau_L$ and thus may lead to numerical diffusion of the FDF field if applied universally. Thus, we set $\beta = 3$ which may lead to a slight over-prediction of sub-Lagrangian-filter variance at some locations but will avoid excessive numerical diffusion which degrades the mean field. Incorporating the above modeling for $\chi$ and $\widetilde{f_L'^2}$, the mixing time scale becomes

$$\tau_L = C_L^{-1} \frac{\beta d_{\tilde{f}}^2}{\Delta_E^2 \nabla\tilde{f} \cdot \nabla\tilde{f}} \tau_E. \tag{34}$$

If particles $p$ and $q$ are located in different Eulerian grid cells, then $\tau_L^p$ and $\tau_L^q$ may vary significantly depending on the differences in $\Delta_E$, $\nabla\tilde{f}$, and $\tau_E$ at those locations. Taking the average of $\tau_L^p$ and $\tau_L^q$ is the logical choice but it can lead to excessive numerical diffusion in some cases. To avoid this, $\tau_L^{p,q}$ is taken as the maximum of $\tau^p$ and $\tau^q$.

## IV. DENSITY COUPLING

Two way coupling occurs between the simulated LES and FDF fields. The LES, computed on an Eulerian grid, provides velocity, turbulent diffusivity, and reference mixture fraction to the Lagrangian FDF scheme which in-turn provides density feedback to the LES. This feedback uses a conditional form[18] of the equivalent enthalpy method which was first developed by Muradoglu *et al.*[22] and later applied for intensive-Lagrangian FDF simulations by Raman *et al.*[10,11] An Eulerian transport equation is solved for a filtered enthalpy-like quantity (the equivalent enthalpy) from which density is obtained algebraically. The influence of the stochastic composition is restricted to the source term in the Eulerian equation. The details of the conditional equivalent method are as follows.

The equivalent enthalpy is defined as[22]

$$h_s = \frac{\gamma_0}{\gamma_0 - 1} \mathscr{R} T, \tag{35}$$

where $\gamma_0$ is the ratio of the constant specific heats, $\mathscr{R}$ is the composition dependent gas constant, and $T$ is the gas temperature, taken here as being proportional to the progress variable $Y$. The equivalent enthalpy has dimensions of energy per mass. For a known pressure, the density is a simple algebraic function of $h_s$,

$$\rho = \frac{\gamma_0}{\gamma_0 - 1} \frac{P}{h_s}. \tag{36}$$

The Eulerian filtered equivalent enthalpy, denoted as $\widetilde{h_s^E}$, observes a conventional LES equation,

$$\frac{\partial \bar{\rho} \widetilde{h_s^E}}{\partial t} + \frac{\partial \bar{\rho} \widetilde{u}_i \widetilde{h_s^E}}{\partial x_i} = -\frac{\partial}{\partial x_i}\left(\widetilde{J}_{h_s,i} + J_{h_s,i}^{\mathrm{sf}}\right) + \widetilde{W}_{h_s}, \tag{37}$$

where the closures of the molecular and subfilter turbulent fluxes are in the form of Eqs. (8) and (11). There is also a stochastic equivalent enthalpy calculated on the Pope particles, $h_s^p$, which is a function of the stochastic composition. The influence of $h_s$ on the $\widetilde{h_s^E}$ field is through the source term $\tilde{W}_{h_s}$. Generally, $\tilde{W}_{h_s}$ can be modeled directly from the particle properties,[22] but in sparse simulations, where most of the LES grid-cells do not contain any Pope particles, direct evaluation of $\tilde{W}_{h_s}$ is not possible. Instead $\widetilde{W}_{h_s}$ is modeled as a relaxation term which dynamically matches $\widetilde{h_s^E}$ with an approximation of the FDF filtered equivalent enthalpy, $\widetilde{h_s}$, at the same location. This approximation involves the evaluation of conditional means determined from particle data according to $F(Z;x,t) = \overline{h_s|Z=\eta}$ and used in the LES in the form $F(\tilde{f};x,t)$. The overbar is used to denote that this conditional average is an instantaneous quantity calculated from an ensemble of particles in the near-neighborhood of the location in question, and $\eta$ represents the mixture fraction sample space. Although the use of conditional averages is approximate (conditional fluctuations are neglected), conditioning on the mixture fraction is in line with MMC and CMC philosophies and can be expected to produce reasonably good results for non-premixed combustion. The source term in Eq. (37) is given by

$$\tilde{W}_{h_s} = \bar{\rho} \frac{\hat{h}_s - \widetilde{h_s^E}}{\tau_{\mathrm{rel}}}. \tag{38}$$

Here, $\hat{h}_s = F(\tilde{f})$ and $\tau_{\mathrm{rel}}$ is a relaxation time determined by numerical conditions: excessively small values can cause instabilities, while $\widetilde{h_s^E}$ would deviate from the target value $\hat{h}_s$ for excessively large $\tau_{\mathrm{rel}}$. In this work, $\tau_{\mathrm{rel}}$ is set to approximately ten times the characteristic numerical time step.

## V. CASE CONFIGURATION

### A. The simulated test case

The sparse-Lagrangian FDF model with a generalized MMC closure is quantitatively tested in simulations of a statistically stationary, spatially evolving, turbulent reacting jet. The flow is similar to the conditions used in Colucci *et al.*[3] The flame chemistry is the same as that used by Norris and Pope[43] and Subramaniam and Pope.[23] Section III previously described the chemistry in general terms while the specific details are discussed below.

A central circular jet with a diameter of $D = 5$ mm issues a fuel stream (mixture fraction equal to 1) with a velocity of $U = 100$ m/s. The co-flowing annulus of air (mixture fraction equal to 0) extends radially to $3.5D$ and has a velocity of $0.5U$. The flow domain extends $14D$ in the axial direction. Turbulence is initiated by a low amplitude signal in the inlet boundary velocity. Unless otherwise noted, the reactive region $R$ (see Fig. 1) encompasses all of $Z$-space for $x/D < 5$ (to avoid heavy extinction near the nozzle) but is limited to $0.03 < Z < 0.07$ and $Y > 0.6$ for $x/D > 5$. The stoichiometric mixture fraction is 0.05 which is similar to that of methane.

Both constant density and variable density flows are simulated. The constant density simulations permit an analysis of the model with different parameter settings without altering the velocity field. The density and molecular viscosity are uniform throughout the flow and are adjusted to give a reference Reynolds number, based on $D$ and $U$, of $\mathrm{Re} = 5000$. Although this is a moderate value of Re, the relative magnitude of the subfilter variance is of greater interest as it represents the level of fluctuations which must be modeled. In the shear layer, the maximum ratio of the Eulerian subfilter variance to total variance of mixture fraction is about 12%.

For the variable density flow, the fluid is treated as an ideal gas with gas constant $\mathscr{R} = 0.287$ kJ/kgK and dynamic viscosity of $2.0 \times 10^{-5}$ Ns/m$^2$. Since density coupling has the greatest potential to destabilize the flow solver, choosing constant values of the other gas parameters is a convenient simplification. The progress variable now represents the normalized temperature with $Y = 0$ and $Y = 1$ corresponding to 20 °C and 2000 °C, respectively. The atmospheric pressure is 100 kPa. The reference Reynolds number based on fluid properties at the jet nozzle is 30 000 although the kinematic viscosity increases six-fold at stoichiometric mixtures suggesting a representative Reynolds number closer to 5000. In the shear layer of the variable density jet, the maximum ratio of the Eulerian subfilter variance to total variance of mixture fraction is about 15%.

### B. Modeling and numerical details

The LES equations are solved in the cylindrical coordinate system using the Flowsi code described by Kempf *et al.*[50] For the constant density flow, the equally spaced LES grid has 140 cells in the axial direction, 35 cells in the radial direction, and 32 cells azimuthally. For the variable density flow, the jet decays more slowly in the axial direction and consequently the numerical diffusion relative error is higher than in the much faster decaying constant density case, thus requiring a doubling of the grid resolution in the axial and radial directions. The LES is a numerical scheme[51] in that the filter width is given by the grid size; specifically we set $\Delta_E$ as the cubed root of the grid-cell volume. A second-order central differencing scheme is used for the momentum transport while a nearly second-order total variation diminishing (TVD) scheme is used for the reference mixture fraction equation. All filtered equations are advanced in time using a third-order Runga-Kutta method. Although the density is variable, the Mach number of the flow is relatively low and a predictor-corrector approach is used to advance pressure consistent with continuity.

The FDF spatial transport is governed by Eq. (23) which is integrated using a first-order Euler-Maruyamma approximation[52] with LES quantities estimated at the particle locations by tri-linear interpolation. The number of Pope particles is set proportionally to the number of LES grid-cells. Results are presented for 20 particles per grid-cell (the intensive case) denoted as 20L/1E, 1 particle per 8 grid-cells denoted as 1L/8E and 1 particle per 27 grid-cells denoted as 1L/27E. For the intensive case, unless otherwise noted, modified Curl's mixing is used; particle mixing pairs are selected randomly from within each LES grid-cell and compositional localness is not otherwise controlled. The mixing time scale for the intensive simulation is given by $\tau_L = \tau_E$. For the sparse simulations, 1L/8E and 1L/27E, generalized MMC mixing is used with three different values of $f_m$, namely $f_m = 0.06$, 0.04, and 0.02. The nominal particle spacing, $\Delta_L$, is a local parameter which, like the Eulerian grid size, increases with the radius. In the shear layer it is approximately 1 mm and 1.4 mm for the 1L/8E and 1L/27E simulations, respectively. The corresponding Eulerian filter size in the shear layer is $\Delta_E \simeq 0.5$ mm.

The time increment is determined by the Courant-Friedrichs-Levy stability criterion that $\max(u\Delta t/\Delta_E) \leq n_{\mathrm{CFL}}$. The same time increment is applied to both the Eulerian and Lagrangian systems. For most simulations in the present work $n_{\mathrm{CFL}} = 0.7$. An additional simulation is performed with $n_{\mathrm{CFL}} = 0.35$ to test the sensitivity to the numerical time step.

Density coupling requires the evaluation of conditional means $\overline{h_s|Z=\eta}$ which are determined from the ensemble of particles in the near-neighborhood of the location being considered. Calculation of $\overline{h_s|Z}$ directly from instantaneous particle data will have a large stochastic error unless the ensemble volume is unrealistically large. Conditional mean profiles of $\hat{h}_s$ are instead selected from a pre-computed table of approximate conditional average curves as shown schematically in Fig. 3. $\hat{h}_s$ is the ordinate of the curve when the abscissa is $\tilde{f}$. The conditional curve which best matches the local particle field is the one with minimal variance relative to the particles. The profile shapes of the pre-computed curves should be similar to the conditional average profiles predicted by the particles and could be determined in a variety of ways including from experimental or previous simulation data.

Weighted particles are used to ensure the desired resolution at all locations regardless of cell mass. The domain is divided into particle-number control cells which contain multiples of the LES grid-cells in the axial, radial,

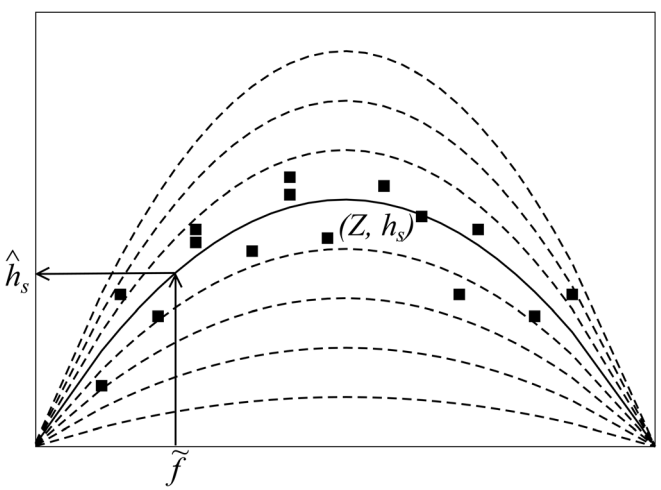


FIG. 3. Schematic showing how $\hat{h}_s$ in Eq. (38) is calculated. The conditional average profile through the ensemble of particle compositions $(Z^p, h_s^p)$ is approximated by a smooth curve selected from a pre-computed table.

and azimuthal directions. The control cells sizes are for case 20L/1E—(1 axial LES cell, 1 radial LES cell, 1 azimuthal LES cell); case 1L/8E—(1,1,32); and case 1L/27E—(5,5,32). The control cells are used only for maintaining the desired particle number and for defining the extent of the particle ensemble for calculating $\hat{h}_s$ (see previous paragraph).

Results are analyzed using both instantaneous and Reynolds averaged quantities; the latter are equivalent to time-averages in this statistically stationary flow and are evaluated from a discrete time-series of approximately 2000 instantaneous images of the field collected over a time of approximately 15 domain flow-throughs. Although the time-averaging of more sparse simulations is based on fewer instantaneous data points our tests confirm that, apart from some additional smoothness, results do not change with a doubling of the simulated time. Unless otherwise noted, an ensemble domain of width $\Delta_E$ is used for evaluation of the moments of the FDF.

## VI. RESULTS

The analysis examines the structure of the mixing model localization, consistency between the LES and FDF passive scalar fields, and comparison to the known exact solution for the single reactive scalar. The sensitivities of FDF predictions to different particle spacing and mixing localization parameters (i.e., $f_m$ and $r_m$) and to some numerical parameters are explored in detail.

### A. Localization structure

The model has one localization parameter which must be defined explicitly, namely $f_m$. This quantity is a characteristic distance in $\tilde{f}$-space between mixing particles and is used to define the quantity $\hat{d}^2_{p,q}$ in Eq. (29). We will see in the following subsections that the value assigned to $f_m$ does not significantly affect the consistency between the FDF and LES mixture fraction fields but that reactive scalar predictions are strongly sensitive to $f_m$. The other localization parameter, $r_m$, is a characteristic distance between mixing particles in physical space. It is a global parameter calculated according to Eq. (28) based on the flow properties in the shear layer at the nozzle exit. Therefore, we should observe that the mean mixing distances at the shear layer at the nozzle exit are $\langle d_{\tilde{f}} \rangle = f_m$ and $\langle d_{\boldsymbol{x}} \rangle = r_m$. (The averaging symbol $\langle \cdot \rangle$ denotes averaging over time and around the azimuthal direction.) Table I indicates that the degree of correspondence between $\langle d_{\tilde{f}} \rangle_{\mathrm{SL}}$ (SL = shear layer) and $f_m$ is generally quite good. While the correspondence between $\langle d_{\boldsymbol{x}} \rangle_{\mathrm{SL}}$ and $r_m$ is less satisfactory (the actual distance tends to be greater by approximately 0.5 mm), the correct trend is observed. This small discrepancy between $\langle d_{\boldsymbol{x}} \rangle_{\mathrm{SL}}$ and $r_m$ may be explained by the likely incorrect assumption that the distance between mixing particles is isotropic (i.e., $r_i = r_m/\sqrt{3}$ in Eq. (29)). Table I also contains data for the intensive simulation 20L/1E. Since modified Curl's model is used for that case $f_m$ is not a free parameter but the distances between mixing particles are never-the-less important to the outcome of the simulation. It can be seen that $\langle d_{\tilde{f}} \rangle_{\mathrm{SL}}$ for 20L/1E is quite large relative to the sparse simulations despite the much smaller value of $\langle d_{\boldsymbol{x}} \rangle_{\mathrm{SL}}$.

TABLE I. Mean mixing distance between mixing particles in the shear layer at the nozzle exit in $\tilde{f}$ and $x$-spaces as a function of $f_m$ and $r_m$.

| Case | $f_m$ | $\langle d_{\tilde{f}} \rangle_{\mathrm{SL}}$ | $r_m$ (mm) | $\langle d_{\boldsymbol{x}} \rangle_{\mathrm{SL}}$ (mm) |
|---|---|---|---|---|
| 20L/1E | — | 0.14 | — | 0.30 |
| 1L/8E | 0.020 | 0.015 | 2.0 | 2.5 |
| | 0.040 | 0.038 | 1.4 | 2.1 |
| | 0.060 | 0.064 | 1.2 | 1.7 |
| 1L/27E | 0.020 | 0.017 | 3.6 | 3.9 |
| | 0.040 | 0.034 | 2.5 | 3.1 |
| | 0.060 | 0.076 | 2.1 | 2.5 |

Figures 4 and 5 show 2D planar images of $\langle d_{\tilde{f}} \rangle$ and $\langle d_{\boldsymbol{x}} \rangle$, respectively. The obvious effect of reducing $f_m$ (right to left in the figures) is to yield lower particle mixing distances in $\tilde{f}$-space while increasing the mixing distances in $x$-space. Comparing the results for 1L/8E and 1L/27E, it can be seen that for a given value of $f_m$ the value of $\langle d_{\boldsymbol{x}} \rangle$ increases when fewer particles are used. Thus of all the simulation cases the greatest values of $\langle d_{\boldsymbol{x}} \rangle$ (of the order of 3.5 mm) occur in the shear layer for 1L/27E with $f_m = 0.02$. Further downstream, where scalar gradients are smaller, lower values of $\langle d_{\tilde{f}} \rangle$ and $\langle d_{\boldsymbol{x}} \rangle$ are observed in all the simulations. Fig. 6 shows the shear layer axial profile of $\langle d_{\boldsymbol{x}} \rangle$. In order to gauge the magnitude of the particle mixing distance, and mindful that the sparse-Lagrangian scheme should resolve the large scale eddies while modeling their dissipation, we should consider its value in relation to the nozzle radius (2.5 mm) which is the upper limit of the integral length scale. Figs. 5 and 6 indicate that $\langle d_{\boldsymbol{x}} \rangle$ is larger than 2.5 mm over most of the shear layer region for simulation 1L/27E with $f_m = 0.02$ and for at least the first few jet diameters downstream of the nozzle for 1L/27E with $f_m = 0.04$ and 1L/8E with $f_m = 0.02$. We note, however, that the nominal shear layer particle spacing, $\Delta_L$, which is the distance between particles without considering which particles mix, is only 1 mm and 1.4 mm for 1L/8E and 1L/27E, respectively. Therefore, while there are sufficient FDF particle numbers to resolve the large-scale eddies, the assumption that the particle mixing time, $\tau_L$, can be based on inertial range scaling may not be completely accurate. We will see in Sec. VI B that, despite this deficiency, the FDF predicts a scalar mixing field which is largely consistent with the LES mixing field.

A quantitative comparison of mixing distances in $\tilde{f}$-space is found in Fig. 7 which shows radial profiles of $\langle d_{\tilde{f}} \rangle$ at three different axial stations. The results demonstrate the ability of the localization scheme to match the mixing distance in $\tilde{f}$-space for 1L/8E and 1L/27E despite the different numbers of particles used. The usefulness of this is demonstrated below when presenting the reactive scalar predictions.

### B. Consistency of the sparse-Lagrangian FDF and the LES in the constant density flow

The consistency between the FDF with an intensive-Lagrangian numerical scheme and the LES equations for

filtered scalar transport has been demonstrated, by others, in both constant density[3] and variable density[4] reacting flows. The purpose of this section is to demonstrate that the consistency can also be maintained using a sparse-Lagrangian model for the joint-scalar FDF. Here, we analyze consistency of the mixture fraction fields in the constant density flow and in Sec. VI D, the same is done for the variable density flow.

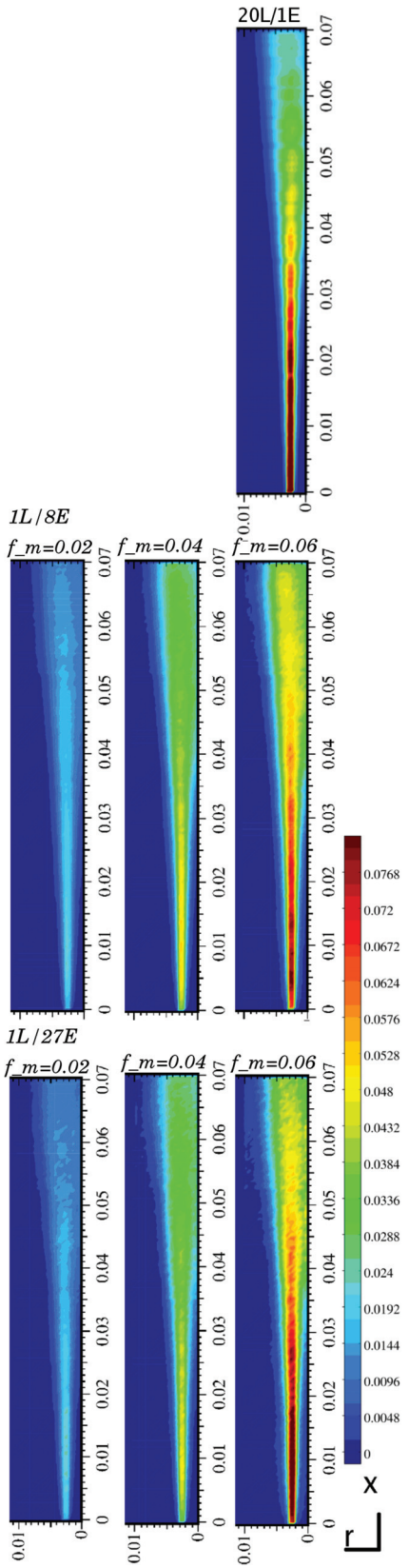


FIG. 4. (Color online) 2D planar images of the mean distance in $\tilde{f}$-space between mixing particles. The right-hand edge of each figure is the jet axis. Axial and radial dimensions are in metres.

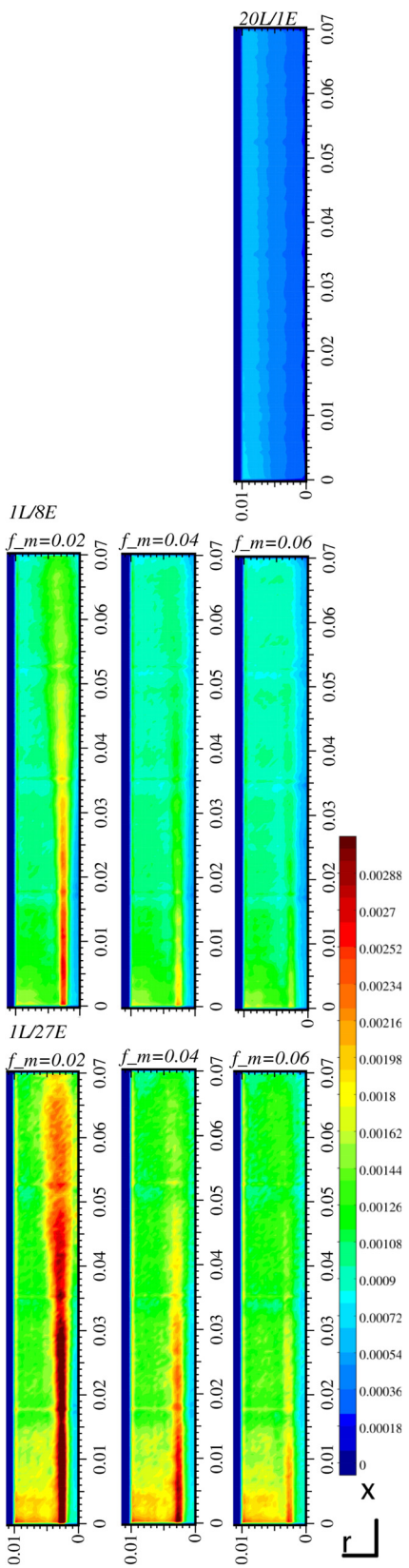


FIG. 5. (Color online) 2D planar images of the mean distance in $x$-space between mixing particles. The right-hand edge of each figure is the jet axis. Mixing distance and axial and radial dimensions are in metres.

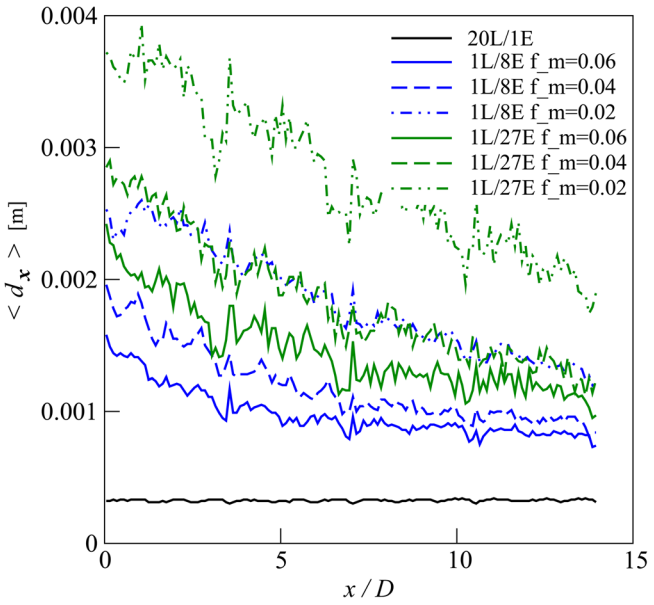


FIG. 6. (Color online) Mean mixing distance in $x$-space along the shear layer at $r/D = 0.5$.

First, we analyze the instantaneous mixture fraction fields. Figure 8 shows planar images of the instantaneous filtered mixture fraction for both the LES and the two sparse FDF schemes with $f_m = 0.06$. The observation scale for calculating the filtered quantity is equal to $\Delta_E$, $5\Delta_E$, and $7\Delta_E$ in the top, middle, and bottom figures, respectively. Obviously,

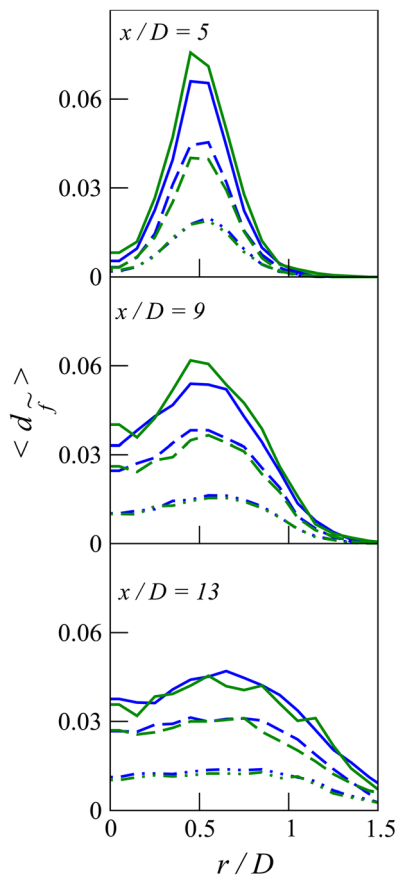


FIG. 7. (Color online) Radial profiles of mean distance in $\tilde{f}$-space between mixing particles. Legend as per Fig. 6.

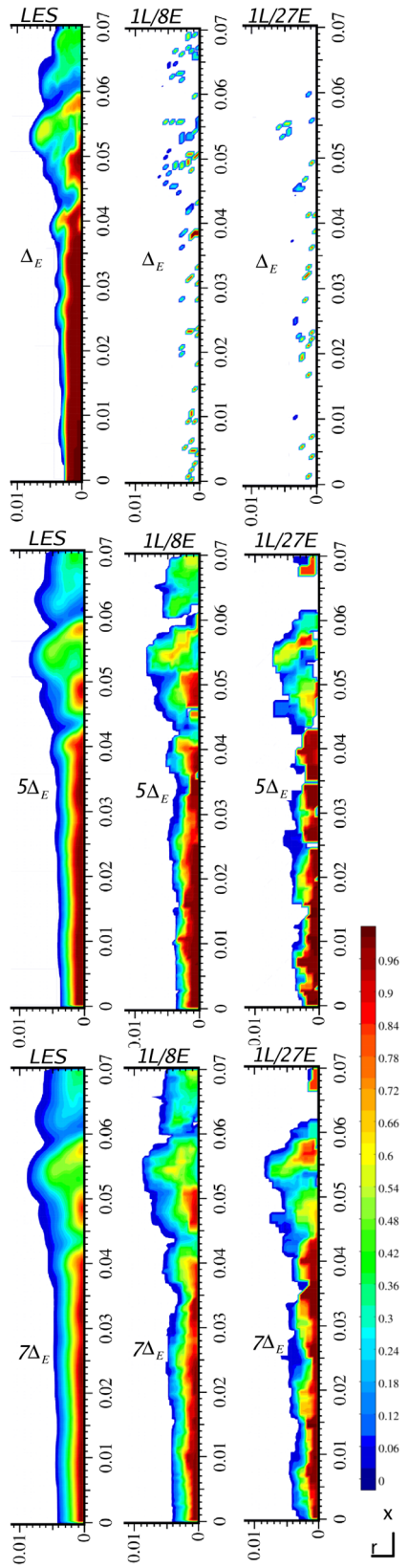


FIG. 8. (Color online) 2D planar images of the filtered mixture fraction obtained from LES, 1L/8E FDF with $f_m = 0.06$ and 1L/27E FDF with $f_m = 0.06$. The observation scale for evaluating the filtered quantity is $\Delta_E$ (top), $5\Delta_E$ (middle), and $7\Delta_E$ (bottom). The right-hand edge of each figure is the jet axis. Axial and radial dimensions are in metres.

when a sparse distribution of particles is used, it is not possible to calculate the filtered value observed at the $\Delta_E$ scale at very many locations, and at the locations where a finite value is calculated, there is a large stochastic error. When the observation scale is increased to include more particles in the ensemble, the FDF filtered mixture fraction fields begin to more closely resemble the LES field (filtered over the same observation scale), although even for the $7\Delta_E$ observation scale notable differences remain, especially for the very sparse 1L/27E case. These differences are attributed to stochastic error which is linked to the number of particles in the ensemble. For an observation scale of $5\Delta_E$, there are on-average about 16 particles in the ensemble for the 1L/8E simulation and 5 particles in the ensemble for the 1L/27E simulation. When the observation scale is increased to $7\Delta_E$ those particle numbers increase to 43 and 13.

A comparison of the Reynolds averaged LES and FDF mixture fraction fields is presented in Fig. 9 which shows radial profiles of the mean and rms at three axial locations. Generally the FDF mean fields are in good agreement with the LES mean field and, furthermore, there is only a relatively small level of sensitivity to the number of particles used. There is stochastic noise apparent near the jet axis which increases with the sparseness of the simulations. There is also a small amount of bias error in the FDF simulations, which appears as an over-prediction of the mixture fraction near the centerline for $x/D > 10$, for both 1L/8E and 1L/27E with $f_m = 0.04$ and 0.02. This bias error is caused by enforcing localization in $\tilde{f}$-space (small $d_{\tilde{f}}$) while permitting $d_x$ to increase beyond the integral length scale (see discussion in Sec. VI A). This results in particles downstream being preferentially influenced by particles from upstream eddies. Importantly, the bias error does not appear for the intensive case, 20L/8E, nor either of the sparse FDF simulations with $f_m = 0.06$ when localization is $\tilde{f}$-space is less strictly enforced and $d_x$ remains smaller than the integral length scale. Numerical diffusion is also evident in the mean result obtained for 1L/8E with $\tau_L = \tau_E$ (shown as a red line in Fig. 9 in the online version of the paper). For sparse simulations, $\tau_L$ is normally scaled relative to $\tau_E$ according to Eq. (34). For $d_x > \Delta_E$, the scaling factor, $C_L^{-1}\beta d_{\tilde{f}}^2/\Delta_E^2 \nabla\tilde{f}\cdot\nabla\tilde{f}$, is typically greater than one and so the subsequent increase in $\tau_L$ relative to $\tau_E$ compensates for the increase in numerical diffusion which occurs if the scaling is not applied.

Radial profiles of the total rms are also shown in Fig. 9. The LES value is given by the square root of the sum of the resolved and subfilter variances, $\langle f_E'^2\rangle^{\frac{1}{2}} = (\langle \widetilde{f_E}'^2\rangle + \langle \widetilde{f_E'^2}\rangle)^{\frac{1}{2}}$, where $\widetilde{f_E'^2}$ is modelled according to Eq. (31). We have chosen to present total rather than subfilter rms since the former is a physical quantity whose consistency between the FDF and LES is of greatest interest and furthermore it can be evaluated locally at an observation scale of $\Delta_E$, even for sparse particle distributions. It is, of course, possible to observe subfilter variance over scales that correspond to the inter-particle distance but that does not change the magnitude of the total rms; as the subfilter variance increases with length, the resolved variance decreases such that the total variance remains unchanged. The mixture fraction total rms results in Fig. 9 reveal a very low sensitivity to the number of particles used in the simulations and also very low sensitivity to the value of $f_m$ with only very minor differences apparent

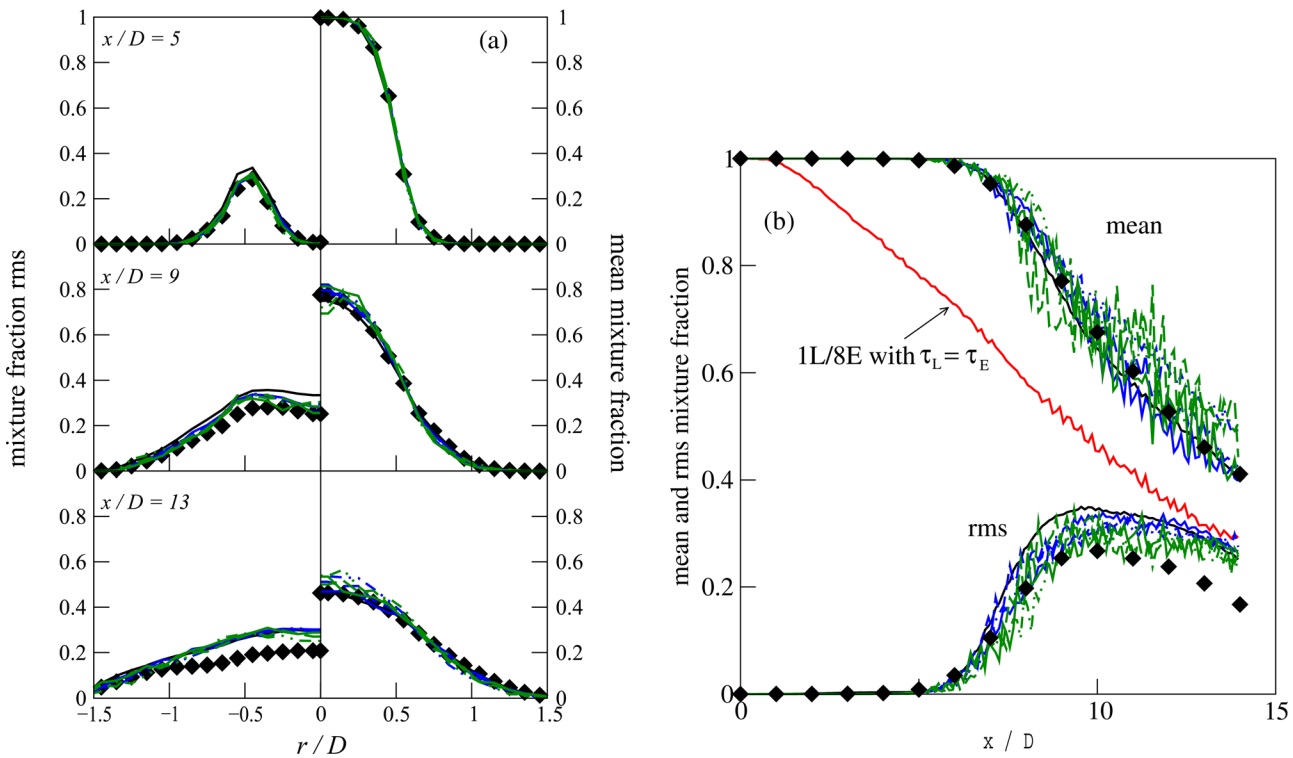


FIG. 9. (Color online) Radial (left) and axial (right) profiles of the average and rms of mixture fraction. Symbols, LES; lines, FDF results denoted as per Fig. 6. An additional FDF result is included for 1L/8E with $\tau_L = \tau_E$.

between the various results. While there is good qualitative agreement between the FDF and LES fields, there is also a systematic relative over-prediction of the FDF rms at all locations and particularly near the centreline at locations far downstream of the nozzle. The presence of this quantitative inconsistency is not unexpected; similar discrepancies are reported in previous FDF publications.[9,10] Inspection of the LES subfilter variance, $\widetilde{f_E'^2}$, reveals that even at its peak relative magnitude, it accounts for only 2% or 3% of the total rms. Therefore, we believe that the inconsistency occurs due to differences in the resolved scale fluctuations of the LES and FDF fields. Note that the intensive case also gives a higher FDF mixture fraction rms. The transport equation terms most responsible for the generation of resolved scale variance, the resolved convective fluxes, are modeled differently in the LES and FDF schemes. In the FDF, the convective flux is conditionally averaged (viz. Eq. (18)) and closed via a gradient diffusion model (viz. Eq. (19)) which does not appear in the LES mixture fraction equation. It is noted, however, that the unconditional convective flux is the same in both the FDF and LES.[3] It is beyond the scope of the current work to quantify and remove these inconsistencies which are not specific to sparse-Lagrangian FDF simulations. Moreover, comparison with experimental data[18] indicates that the LES total rms is often significantly affected by numerical diffusion and therefore the FDF prediction may be more accurate.

An alternative view of the correlation between the FDF and LES simulated mixture fraction fields is given in Figs. 10 and 11 which show scatter plots of instantaneous $Z^p$ versus $\tilde{f}^p$ at $x/D=9$ for the intensive simulation with modified Curl's mixing and two sparse simulations cases with $f_m=0.02$, 0.04, and 0.06. The bias error caused by preferential axial diffusion, discussed above in the context of the mean mixture fraction fields, is evident for sparse simulations with $f_m=0.02$ in the form of the non-linear shape of the scatter plots near the ends. Overall, however, there is a clear correlation between the $Z$ and $\tilde{f}$ fields, and this correlation improves when $f_m$ is reduced so that mixing is more local in $\tilde{f}$-space. In MMC terminology, the quantity $Z-\langle Z|\tilde{f}=\eta\rangle$ is called a minor fluctuation (i.e., the fluctuation with respect to the average conditioned on the reference variable). Minor fluctuations are the quantities directly controlled by the MMC mixing model and their magnitude cannot be controlled at length scales smaller than the distance between mixing particles. Therefore, the minor fluctuations are not as locally controlled when a more sparse distribution of Pope particles is used. This explains the increasing level of minor fluctuations from top to bottom of Fig. 11. The scatter plot for the intensive simulation with modified Curl's mixing shown in Fig. 10 indicates that even when the distance between mixing particles is very small, there can still be quite large fluctuations of $Z$ with respect to $\tilde{f}$ if the mixing model is not local. In sparse simulations, the loss of control at the small scales can however be offset by decreasing $f_m$; effectively using the well resolved LES reference mixture fraction, $\tilde{f}$, to localize mixing thus providing a level of control of the fluctuations that is not possible with non-local mixing models.

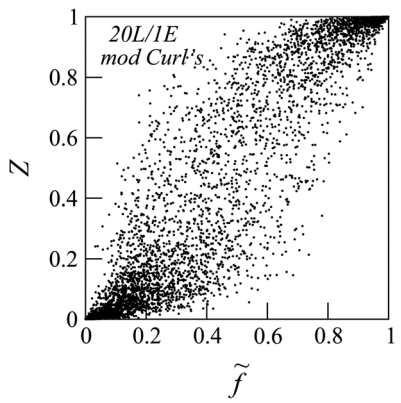


FIG. 10. Scatter plots of instantaneous $Z^p$ versus $\tilde{f}^p$ at $x/D=9$ for the intensive simulation 20L/1E with modified Curl's mixing. Approximately 10 000 particle sample points are displayed.

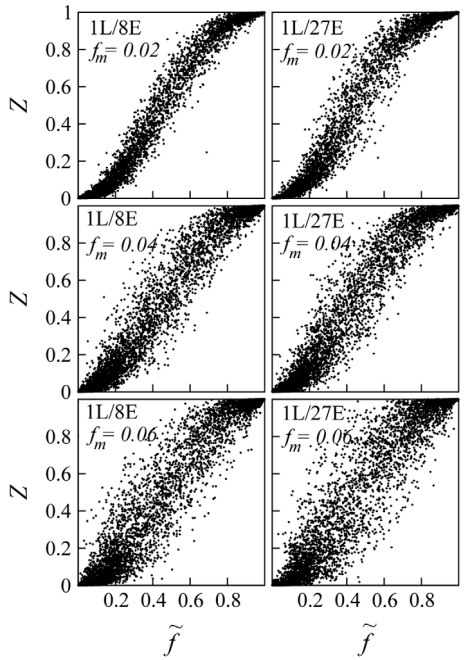


FIG. 11. Scatter plots of instantaneous $Z^p$ versus $\tilde{f}^p$ at $x/D=9$ for the sparse simulations with varying $f_m$. Approximately 10 000 particle sample points are displayed in each scatter plot.

### C. Reactive scalar predictions in the constant density flow

We now analyze the FDF predictions of the reactive scalar, $Y$, in comparison to the equilibrium (exact) flamesheet composition. Figs. 12 and 13 show scatter plots of $Y$ versus $Z$ at $x/D=9$ for the constant density flow. The intensive simulation using modified Curl's model (Fig. 12) indicates that for FDF models with non-local mixing, even those with many closely-spaced particles, there can be significant departures from the equilibrium solution. A result is also shown for 20L/1E with MMC mixing with $f_m=0.02$. The clear effect of the localization in $\tilde{f}$-space is a significant reduction in the number of departures from the equilibrium flamesheet.

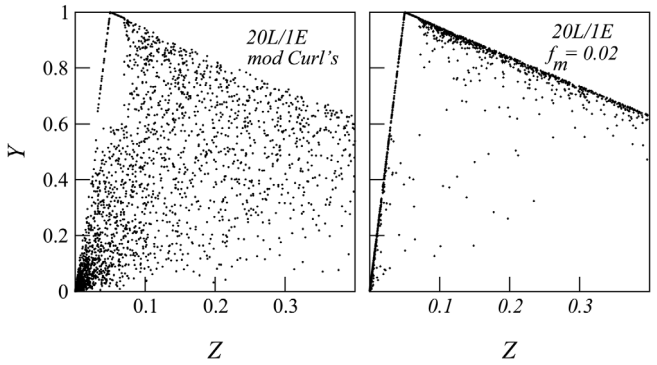


FIG. 12. Scatter plots of instantaneous $Y^p$ versus $Z^p$ at $x/D = 9$ for the intensive simulation 20L/1E with modified Curl's mixing (left) and MMC mixing with $f_m = 0.02$ (right). Approximately 8000 particle sample points are displayed in each scatter plot.

We note that the use of the filtered $\tilde{f}$ field for localization of intensive FDF simulations is not fully justifiable since the particle spacing is much smaller than the filter width applied to the LES mixture fraction. It is possible to include some subfilter fluctuations to the reference mixture fraction field to overcome this issue but that is a new model that is beyond the scope of the current work. The level of conditional fluctuations shown in Fig. 12 for $f_m = 0.02$ is small but some fluctuations still exist. Although the mixing distance in $\tilde{f}$-space for this case is thinner than the width of the stoichiometric reaction zone, the distance in $Z$-space may not always be so; this is because of the independence of the reference mixture fraction, $\tilde{f}$, and the composition mixture fraction, $Z$.

We now concentrate on the main focus which is the application of MMC to sparse FDF simulations. The results for the sparse simulations with MMC mixing show that the level of conditional fluctuations is strongly dependent on $f_m$, with smaller $f_m$ (from bottom to top in Fig. 13) leading to fewer departures from the equilibrium composition and thus a more accurate prediction. Even when $f_m$ is set to as large as 0.06, the level of fluctuations in the sparse simulations is still smaller than for the intensive simulation with modified Curl's mixing. Although not exactly the same, the level of conditional fluctuations is similar between simulation cases 1L/8E and 1L/27E when the same value of $f_m$ is used, suggesting a strong correlation between conditional variance and the distance between mixing particles in the reference mixture fraction space.

Figure 14 shows conditional average and conditional rms profiles corresponding the sparse simulation scatter plots discussed in the previous paragraph. Conditional profiles are also shown further downstream at $x/D = 13$. The black lines in the figures indicate the equilibrium solution. It is seen that the FDF results approach the equilibrium composition with decreasing $f_m$ and for $f_m = 0.02$ the conditional mean for both 1L/8E and 1L/27E is quite accurate although it is slightly less accurate at $x/D = 13$ than at $x/D = 9$ since the fluctuations have had more time to accumulate. The equilibrium conditional rms is, of course, zero but the FDF is unable to achieve this low value. While still smaller values of $f_m$ would reduce the conditional rms below what is shown in Fig. 14, the FDF conditional variance will always remain finite due to the independence of the $\tilde{f}$ and $Z$ fields and thus imperfect localization in $Z$-space. The similarity between the conditional profiles for 1L/8E and 1L/27E for a given value of $f_m$ is clearly evident in the figures and this impressive outcome demonstrates the possibility of achieving equivalent reactive scalar statistics even when the number of particles (and hence computational cost) is significantly reduced.

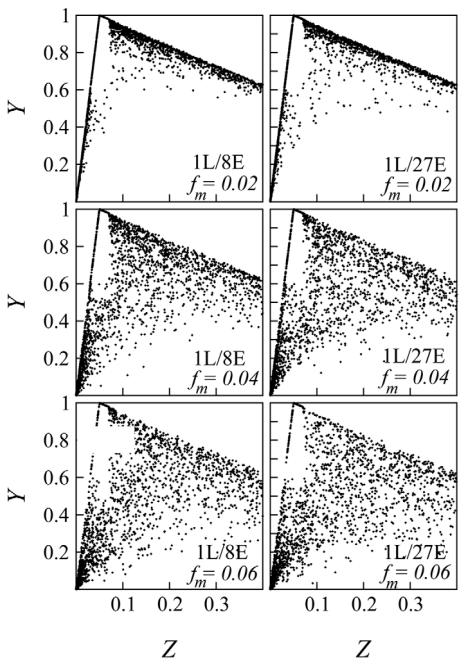


FIG. 13. Scatter plots of instantaneous $Y^p$ versus $Z^p$ at $x/D = 9$ for the sparse simulations with varying $f_m$. Approximately 8000 particle sample points are displayed in each scatter plot.

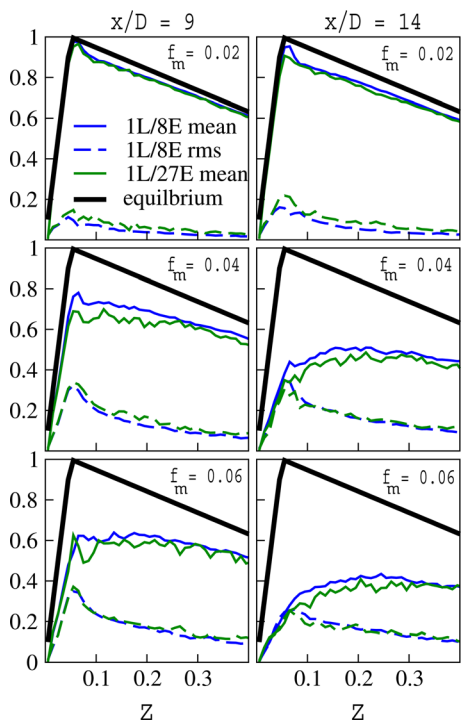


FIG. 14. (Color online) Profiles of conditional average (solid lines) and conditional rms (dashed lines) of $Y$ with varying $f_m$.

The trends in the reactive scalar predictions for varying $f_m$ are presented in Fig. 15 showing the burning index (BI) of $Y$ which is the mean of the conditional averages normalized by the equilibrium solution. Here, we average the BI over the whole mixture fraction range whereas others[53] define the BI as the mean within the upper and lower reaction limits. The discontinuity in the reaction rate for the present test case results in significant numerical noise in the near-stoichiometric conditional means (see Fig. 14) and thus a more illustrative comparison is made by averaging over the entire mixture fraction range. This also allows us to compare results for flames with different chemistry (see below). The BI results in Fig. 15 once again demonstrate the strong dependence of the reactive scalar results on $f_m$ and the close similarity between different sparse FDF reactive scalar predictions for a given value of $f_m$. As a point of comparison, the BI for the intensive simulation with modified Curl's mixing is 0.71 and 0.47 at $x/D=9$ and 13, respectively. As discussed above (see Fig. 12), an additional intensive simulation was run using MMC mixing with $f_m=0.02$. The BI results for that case are indistinguishable from the sparse simulation BI results shown in Fig. 15. Intensive FDF results of a partially premixed methane/air flame with a broad reaction zone, presented by Bisetti and coworkers at the Turbulent Nonpremixed Flame Workshop (TNF8, Heidelberg, 2006), have demonstrated little sensitivity to the mixing model and good agreement with experimental data for such flames is possible even when the non-local IEM mixing model is used.[11] The present results demonstrate that for very thin reaction zone chemistry intensive FDF predictions can be inaccurate when a non-local mixing model is used and that MMC is a good model for both sparse and intensive simulations.

Figure 15 also shows the sensitivity of the simulations to variations in the reaction zone width and the numerical time step. A series of results are shown for 1L/8E when the stoichiometric mixture fraction has been increased from $Z_s=0.05$ to $Z_s=0.10$ and the reaction zone width in $Z$-space has been doubled to be $Z_u-Z_l=0.08$. Although it is expected that there is a lower probability of particles mixing across the wider reaction zone, thus leading to fewer departures from the flamesheet and a BI closer to unity, the results show that the sensitivity to a doubling of the reaction zone width is actually quite small and certainly much smaller than the sensitivity to variations in $f_m$. The greatest sensitivity occurs at $x/D=13$ for $f_m=0.04$ where there is a slight but noticeable increase in BI (as expected) for the wider reaction zone case.

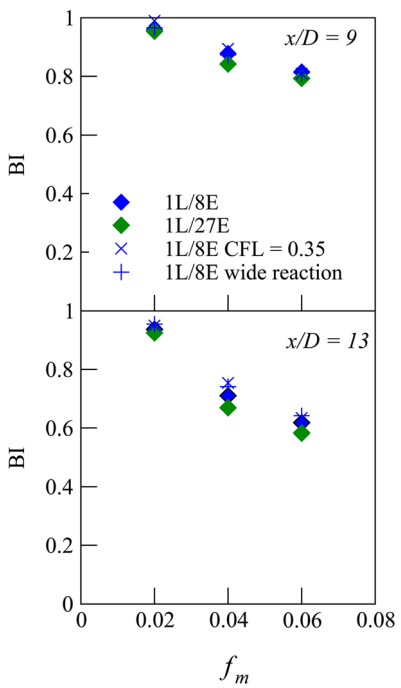


FIG. 15. (Color online) Burning index of $Y$ as a function of $f_m$.

Unfortunately the BI results reveal a small sensitivity to the size of the numerical time step although, for the present case at least, it is much less than the sensitivity to the model parameter $f_m$. The time step tests are performed for 1L/8E only. When the time step is halved by reducing the CFL number from 0.7 to 0.35, the BI increases most obviously at $x/D=9$ when $f_m=0.04$. Results for $f_m=0.02$ and 0.06 and generally at $x/D=13$, the sensitivity to the time step is quite small. Note that only the reactive species is dependent on the numerical time step. The FDF mixture fraction fields are almost indistinguishable whether $n_{\mathrm{CFL}}=0.35$ or 0.70. Such dependence of reactive species conditional variances on the numerical time step is a common feature among the most commonly used PDF mixing models[44] and the present results show that the same is true for MMC.

The analysis has shown the strong dependence of the reactive species predictions on the input parameter $f_m$, increasing $f_m$ results in greater conditional fluctuations. It is not possible from the current work to determine the optimal value of $f_m$ in general. For the present test case, the correct result is $\mathrm{BI}=1$ and this is achieved reasonably well, although not perfectly, by setting $f_m=0.02$. In turbulent flames of practical interest, there is always some level of conditional variance. Sparse-Lagrangian FDF simulations of Sandia Flame E (Ref. 18) have demonstrated that it is possible, in principle, to select the degree of localization in $\tilde{f}$-space to match experimental data. This method of controlling conditional variance is quite intuitive; increased levels of conditional fluctuations result when the composition space is not fully confined to the mixture fraction manifold, and so, de-localization of the mixing model by increasing the value of $f_m$ is physically realistic.

### D. Consistency of the sparse-Lagrangian FDF and the LES in the variable density flow

Until this point results have been presented for the constant density flow. We now consider the case where the progress variable represents a normalized temperature and density varies according to the ideal gas equation of state. The most stringent test of the density coupling scheme described in Sec. IV is a simulation which has a distribution of particles much sparser than the LES grid and which also exhibits large density fluctuations which could lead to numerical instability if not properly handled. Therefore, the density coupling is demonstrated for simulation 1L/27E with $f_m=0.06$, since this case has the greatest number of LES cells

per particle (i.e., 27) and conditional fluctuations of temperature and hence density are large. In the constant density flow, this simulation case yields a BI of 0.79 and 0.58 at $x/D = 9$ and 13, respectively. In the variable density case, the jet develops differently due to low density along the axis and the BI values are instead 0.62 and 0.45 at those two locations.

Figure 16 shows scatter plots of equivalent enthalpy and density versus the mixture fraction at $x/D = 9$. The left scatter plots are the FDF simulated quantities, $h_s$ and $\rho$ versus $Z$. The middle plots show the target conditional field, $\hat{h}_s$ and its corresponding density $\hat{\rho} = \frac{\gamma_0}{\gamma_0 - 1}\frac{P}{\hat{h}_s}$ versus $\tilde{f}$, towards which the LES equivalent enthalpy, $\widetilde{h}_s^E$, is relaxed according to Eq. (38). The conditionally averaged nature of $\hat{h}_s$ and $\hat{\rho}$ is clearly evident in the plots. The right hand side plots show $\widetilde{h}_s^E$ and the LES filtered density, $\bar{\rho}$, versus $\tilde{f}$. The data points are the instantaneous values at the center of the LES grid-cells. We can assess the consistency of the FDF and LES density fields (and hence the quality of the coupling scheme) by a comparison of the left and right scatter plots in Fig. 16. There is clearly a similarity between the fields although differences are apparent near stoichiometry, which are due to the discontinuity in the FDF reaction rate. The corresponding conditional mean densities for the FDF, $\langle \rho | Z \rangle$, and LES, $\langle \bar{\rho} | \tilde{f} \rangle$, are shown in Fig. 17, which additionally shows results at $x/D = 5$ and $x/D = 13$. Clearly, there is a very good level of consistency between the conditional mean density fields.

Radial profiles of the LES and FDF predicted Reynolds average and rms of mixture fraction are shown in Fig. 18. As for the constant density flow, the agreement between the mean quantities is very good, although the LES field exhibits some numerical diffusivity while the FDF does not. It is well known that numerical diffusion diminishes with grid size. When the variable density flow is simulated with the coarser grid used for the constant density flow, numerical diffusion is quite excessive and there is very poor consistency between the LES and FDF scalar fields. As for the constant density flow reported above and in other published variable density FDF simulations,[9,10] the FDF predicts higher total scalar rms in the shear layer than does the LES. Possible explanations are already given in Sec. VI B. Despite these relatively minor quantitative inconsistencies, qualitative agreement is very good.

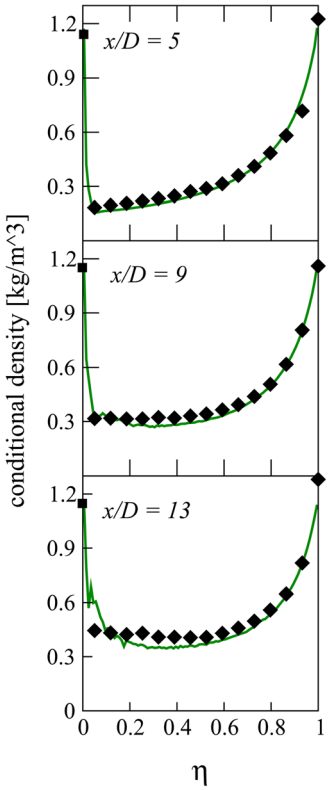


FIG. 17. (Color online) Conditional average profiles of density versus mixture fraction in the variable density flow. Symbols, LES; lines, 1L/8E with $f_m = 0.06$.

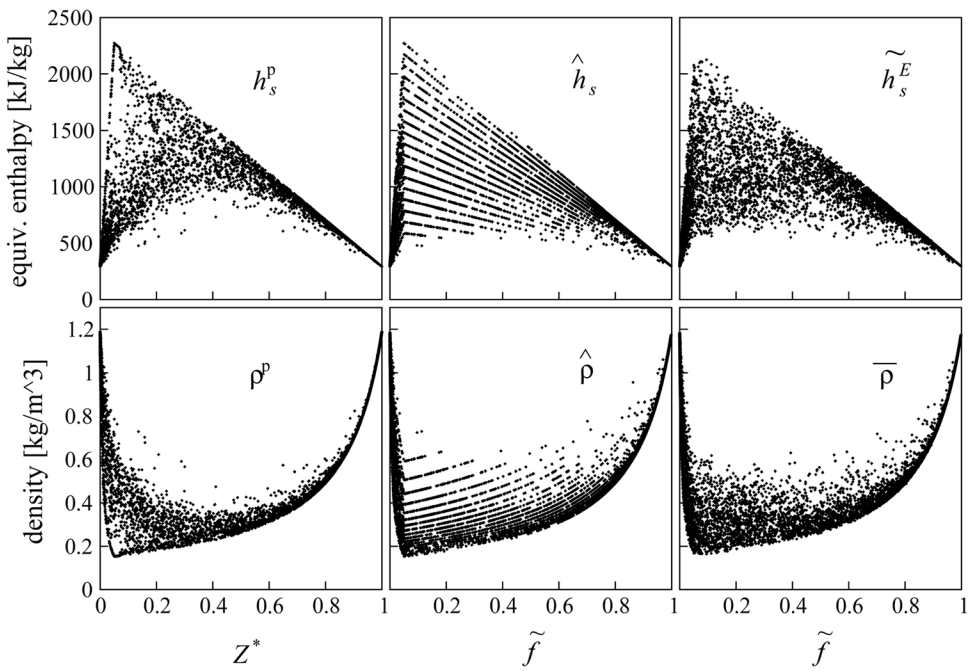


FIG. 16. Scatter plots of instantaneous equivalent enthalpy (top) and density (bottom) versus mixture fraction at $x/D = 9$ in the variable density flow. Approximately 10 000 particle sample points are displayed in each scatter plot.

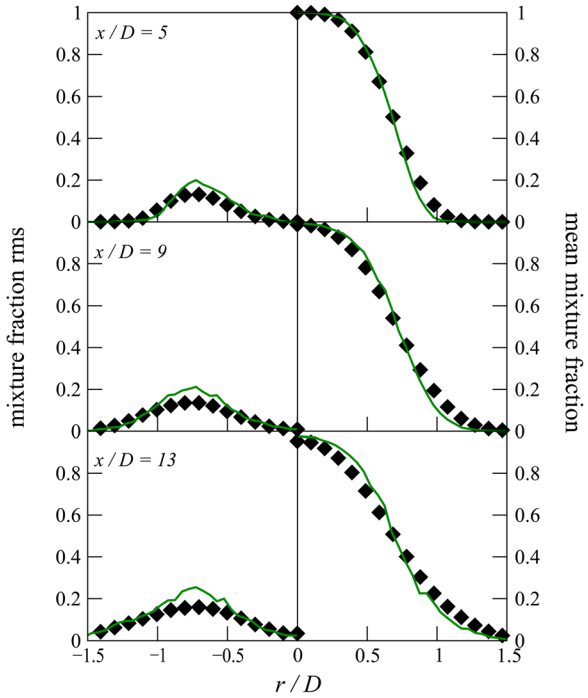


FIG. 18. (Color online) Radial profiles of the average mixture fraction in the variable density flow. Symbols, LES; lines, 1L/8E with $f_m = 0.06$.

Finally the Reynolds averaged density fields by both the LES and FDF simulations are presented in Fig. 19. There are significant differences between the fields especially in the outer part of the shear layer. These discrepancies are due to the differences between the LES and FDF mixture fraction fields evident in Fig. 18. Our density coupling method is consistent at the level of conditional mean density but due to the large density gradient in mixture fraction space on the lean side of stoichiometry, small differences between the LES and FDF filtered mixture fraction fields can lead to large mean density differences.

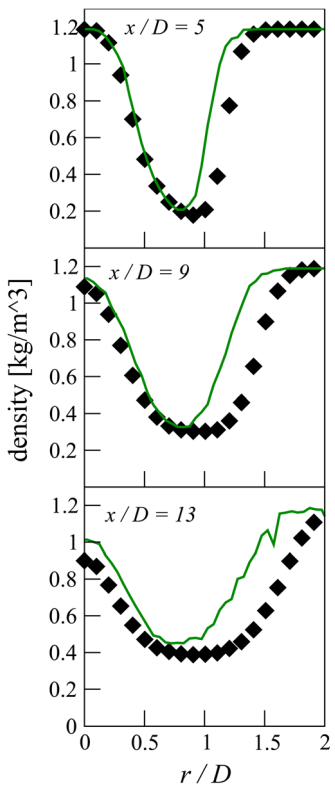


FIG. 19. (Color online) Radial profiles of the average density in the variable density flow. Symbols, LES; lines, 1L/8E with $f_m = 0.06$.

## VII. CONCLUSION

A detailed quantitative analysis is presented of sparse-Lagrangian FDF simulations in constant density and variable density reacting jets. Sparse-Lagrangian simulations, theoretically developed and tested against a number of experimental jet flames over the past few years, have the advantage of very low computational cost compared to more traditional intensive-Lagrangian FDF simulations. Accurate and consistent simulation using a sparse-Lagrangian scheme requires a model that, in the absence of close physical space proximity between particles, enforces mixing localness in composition space while preserving the principles of good mixing. Additionally the model should treat density coupling between the FDF evaluated at relatively few discrete particle locations and the more highly resolved LES in a way that is both accurate and numerically stable. The MMC model enforces mixing to be local in an independent reference space. Here, as in other sparse-Lagrangian publications dealing with non-premixed combustion, we use a generalized MMC model whereby the reference space is given by the LES filtered mixture fraction. Thus, the model enforces a CMC-type closure on an FDF model, unifying the two methods. Density coupling between the FDF and LES fields is achieved through an adaptation of the equivalent enthalpy method which is consistent at the level of the conditional mean densities. The LES density is evaluated directly from a filtered equivalent enthalpy which is related to the FDF through a source term which relaxes the LES field to the FDF conditional mean.

The simulated flows consist of a circular fuel jet within an air coflow and the combustion chemistry is modeled as an idealized flamesheet such that the single reactive species is a piecewise linear function of the mixture fraction. Reactions which instantaneously convert the reactive species to its equilibrium value occur only within a very thin reaction zone near stoichiometry. This is a particularly difficult test case for a mixing model since, unless the as-mixed particle compositions fall within the thin reaction zone, non-physical conditional fluctuations will appear. In the constant density flow, the composition field does not affect the flow field, whereas in the variable density flow the reactive species represents temperature and density is modeled through an ideal gas equation of state. Two different sparse particle distributions are used in the simulations; the first uses one Pope particle for every eight LES grid-cells (1L/8E) and the other significantly more sparse simulation uses one Pope particle for every 27 grid-cells (1L/27E). Detailed results are also presented for an intensive-Lagrangian FDF simulation employing 20 particles per LES grid-cell (20L/1E) and using the non-local modified Curl's mixing model. One additional simulation is performed for 20L/1E with MMC mixing to

demonstrate the need for a localized mixing model such as MMC for thin reaction zone chemistry even when many particles are used.

The localization structure of the generalized MMC mixing model is examined in detail. A new parameter $f_m$ has been introduced which is a characteristic distance in LES filtered mixture fraction space between mixing particles. We relate $f_m$ to a characteristic physical distance scale between mixing particles, $r_m$, by considering isoscalar surfaces as fractals. With this model, the particle mixing pair selection algorithm controls the distance in LES mixture fraction space while allowing the physical distance between mixing particles to vary with the sparseness of the particle distribution and the details of the flow field. In regions of the flow with large scalar gradients enforcement of close mixing proximity in mixture fraction space leads to greater mixing distances in physical space.

Consistency between the sparse-Lagrangian FDF and LES mixture fraction fields is presented using instantaneous and Reynold averaged results. Since the FDF is evaluated using only very few particles, the instantaneous filtered mixture fraction is evaluated over an observation scale encompassing a number of LES grid-cells. Through time-averaging, the Reynolds averaged statistics of even very sparse simulation cases can be evaluated locally. It is shown that there is generally very good agreement between the FDF and LES mean mixture fraction fields although for sparse simulations with small values of $f_m$ the large physical distance between mixing particles can lead to bias error caused by preferential axial diffusion. In common with other FDF publications, the mixture fraction rms in the shear layer is relatively over-predicted by the FDF but there is very good qualitative agreement at all locations. The results show that, provided care is taken to avoid bias error, there is very little sensitivity of the FDF mixture fraction fields to variations in the number of particles used in the simulations or to the value of the localization parameter, $f_m$. For the variable density flow, the consistency of the mixture fraction fields is similarly good to the constant density flow. Density coupling is consistent at the level of the conditional mean density and results indicate close similarity between FDF and LES conditional densities.

The reactive scalar predictions are strongly dependent on $f_m$ with larger values yielding more departures from the flamesheet composition and greater conditional variance. The analysis shows that the distance in the LES reference mixture fraction space is the primary parameter affecting the conditional variance. The same reactive composition can be predicted with different sparse particle distributions when $f_m$ is kept constant. The burning index (evaluated over all mixture fraction space) shows only minor sensitivity to a doubling of the reaction zone width but, in common with other common mixing models, there is some dependence on the size of the numerical time step. The optimal value of $f_m$ will likely be chemistry dependent with different fuels exhibiting different reaction zone thickness in mixture fraction space. Although the low sensitivity to this reaction zone width observed for the present case gives some hope that the chemistry dependence is not a dominant factor, the matter will only be clarified by testing of the method for a wide range of fuels and flame conditions.

[1]S. B. Pope, "Computations of turbulent combustion: Progress and challenges," in *Proceedings of the 23rd Symposium (International) on Combustion* (The Combustion Institute, Pittsburgh, 1990), pp. 591–612.
[2]F. Gao and E. E. O'Brien, "A large-eddy simulation scheme for turbulent reacting flows," Phys. Fluids A **5**, 1282 (1993).
[3]P. J. Colucci, F. A. Jaberi, P. Givi, and S. B. Pope, "Filtered density function for large eddy simulation of turbulent reacting flows," Phys. Fluids **10**, 499 (1998).
[4]F. A. Jaberi, P. J. Colucci, S. James, P. Givi, and S. B. Pope, "Filtered mass density function for large-eddy simulation of turbulent reacting flows," J. Fluid Mech. **401**, 85 (1999).
[5]L. Y. M. Gicquel, P. Givi, F. A. Jaberi, and S. B. Pope, "Velocity filtered density function for large eddy simulation of turbulent flows," Phys. Fluids **14**, 1196 (2002).
[6]M. R. H. Sheikhi, T. G. Drozda, P. Givi, and S. B. Pope, "Velocity-scalar filtered density function for large eddy simulation of turbulent flows," Phys. Fluids **15**, 2321 (2003).
[7]M. R. H. Sheikhi, P. Givi, and S. B. Pope, "Velocity-scalar filtered mass density function for large eddy simulation of turbulent reacting flows," Phys. Fluids **19**, 095106 (2007).
[8]X. Y. Zhou and J. C. F. Pereira, "Large eddy simulation (2D) of a reacting plane mixing layer using filtered density function closure," Flow, Turbul. Combust. **64**, 279 (2000).
[9]M. R. H. Sheikhi, T. G. Drozda, P. Givi, F. A. Jaberi, and S. B. Pope, "Large eddy simulation of a turbulent nonpremixed piloted methane jet flame (Sandia Flame D)," Proc. Combust. Inst. **30**, 549 (2005).
[10]V. Raman, H. Pitsch, and R. O. Fox, "Hybrid large-eddy simulation/Lagrangian filtered density function approach for simulating turbulent combustion," Combust. Flame **143**, 56 (2005).
[11]V. Raman and H. Pitsch, "A consistent LES/filtered-density function formulation for the simulation of turbulent flames with detailed chemistry," Proc. Combust. Inst. **31**, 1711 (2007).
[12]T. G. Drozda, M. R. H. Sheikhi1, C. K. Madnia, and P. Givi, "Developments in formulation and application of the filtered density function," Flow, Turbul. Combust. **78**, 35 (2007).
[13]D. C. Haworth, "Progress in probability density function methods for turbulent reacting flows," Prog. Energy Combust. Sci. **36**, 168 (2010).
[14]H. Pitsch, "Large-eddy simulation of turbulent combustion," Annu. Rev. Fluid Mech. **38**, 453 (2006).
[15]A. Y. Klimenko and M. J. Cleary, "Convergence to a model in sparse-Lagrangian FDF simulations," Flow, Turbul. Combust. **85**, 567 (2010).
[16]M. J. Cleary, A. Y. Klimenko, J. Janicka, and M. Pfitzner, "A sparse-Lagrangian multiple mapping conditioning model for turbulent diffusion flames," Proc. Combust. Inst. **32**, 1499 (2009).
[17]M. J. Cleary and A. Y. Klimenko, "A generalised multiple mapping conditioning approach for turbulent combustion," Flow, Turbul. Combust. **82**, 477 (2009).
[18]Y. Ge, M. J. Cleary, and A. Y. Klimenko, "Sparse-Lagrangian FDF simulations of Sandia Flame E with density coupling," Proc. Combust. Inst. **33**, 1401 (2011).
[19]A. Y. Klimenko, "On simulating scalar transport by mixing between Lagrangian particles," Phys. Fluids **19**, 031702 (2007).
[20]A. Y. Klimenko, "Lagrangian particles with mixing. Part 1: Simulating scalar transport," Phys. Fluids **21**, 065101 (2009).
[21]A. Y. Klimenko, "Lagrangian particles with mixing. Part 2: Sparse-Lagrangian methods in application for turbulent reacting flows," Phys. Fluids **21**, 065102 (2009).
[22]M. Muradoglu, S. B. Pope, and D. A. Caughey, "The hybrid method for the PDF equations of turbulent reactive flows: Consistency conditions and correction algorithms," J. Comput. Phys. **172**, 841 (2001).
[23]S. Subramaniam and S. B. Pope, "A mixing model for turbulent reactive flows based on Euclidean minimum spanning trees," Combust. Flame **115**, 487 (1998).
[24]A. Y. Klimenko and S. B. Pope, "A model for turbulent reactive flows based on multiple mapping conditioning," Phys. Fluids **15**, 1907 (2003).
[25]M. J. Cleary and A. Y. Klimenko, "Multiple mapping conditioning: A new modelling framework for turbulent combustion," in *Turbulent Combustion Modelling. Advances, New Trends and Perspectives*, edited by T. Echekki and E. Mastorakos (Springer, London, 2011), pp. 143–171.
[26]S. B. Pope, "PDF methods for turbulent reactive flows," Prog. Energy Combust. Sci. **11**, 119 (1985).

[27]U. Maas and S. B. Pope, "Simplifying chemical-kinetics: Intrinsic low-dimensional manifolds in composition space," Combust. Flame **88**, 239 (1992).
[28]V. Bykov and U. Maas, "The extension of the ILDM concept to reaction-diffusion manifolds," Combust. Theory Modell. **11**, 839 (2007).
[29]A. Y. Klimenko and R. W. Bilger, "Conditional moment closure for turbulent combustion," Prog. Energy Combust. Sci. **25**, 595 (1999).
[30]R. S. Rogallo and P. Moin, "Numerical simulation of turbulent flows," Ann. Rev. Fluid Mech. **16**, 99 (1984).
[31]C. Meneveau and J. Katz, "Scale-invariance and turbulence models for large-eddy simulation," Annu. Rev. Fluid Mech. **32**, 1 (2000).
[32]S. Navarro-Martinez, A. Kronenburg, and F. Di Mare, "Conditional moment closure for large eddy simulations," Flow, Turbul. Combust. **75**, 245 (2005).
[33]O. Stein and A. Kempf, "LES of the Sydney swirl flame series: A study of vortex breakdown in isothermal and reacting flows," Proc. Combust. Inst. **31**, 1755 (2007).
[34]J. Smagorinsky, "General circulation experiments with the primitive equations," Mon. Weather Rev. **91**, 99 (1963).
[35]M. Germano, U. Piomelli, P. Moin, and W.H. Cabot, "A dynamic subgrid-scale eddy viscosity model," Phys. Fluids A **3**, 1760 (1991).
[36]R. L. Curl, "Dispersed phase mixing: I. Theory and effects of simple reactors," AIChE J. **9**, 175 (1963).
[37]J. Janicka, W. Kolbe, and W. Kollmann, "Closure of the transport equation for the probability density function of turbulent scalar field," J. Non-Equil. Thermodyn. **4**, 47 (1979).
[38]C. Dopazo and E. E. OBrien, "An approach to the autoignition of a turbulent mixture," Acta Astronaut **1**, 1239 (1974).
[39]C. M. Cha and P. Trouillet, "A subgrid-scale mixing model for large-eddy simulations of turbulent reacting flows using the filtered density function," Phys. Fluids **15**, 1496 (2003).
[40]D. W. Meyer and P. Jenny, "A mixing model for turbulent flows based on parameterized scalar profiles," Phys. Fluids **18**, 035105 (2006).
[41]D. A. Shetty, A. J. Shandy, and S. H. Frankel, "A new fractal interaction by exchange with the mean mixing model for large eddy simulation/filtered mass density function applied to a multiscalar three-stream turbulent jet," Phys. Fluids **22**, 025002 (2010).
[42]K. Vogiatzaki, A. Kronenburg, S. Navarro-Martinez, and W. P. Jones, "Stochastic multiple mapping conditioning for a piloted, turbulent jet diffusion flame," Proc. Combust. Inst. **33**, 1523 (2011).
[43]A. T. Norris and S. B. Pope, "Turbulent mixing model based on ordered pairing," Combust. Flame **83**, 27 (1991).
[44]A. Y. Klimenko, "Matching conditional moments in PDF modelling of nonpremixed combustion," Combust. Flame **143**, 369 (2005).
[45]A. Kronenburg and M. J. Cleary, "Multiple mapping conditioning for flames with partial premixing," Combust. Flame **155**, 215 (2008).
[46]M. J. Cleary and A. Kronenburg, "Multiple mapping conditioning for extinction and reignition in turbulent diffusion flames," Proc. Combust. Inst. **31**, 1497 (2007).
[47]V. R. Kuznetsov and V. A. Sabelnikov, *Turbulence and Combustion* (Hemisphere, New York, 1990).
[48]K. R. Sreenivasan, "Fractals and multifractals in fluid turbulence," Ann. Rev. Fluid Mech. **23**, 539 (1991).
[49]J. H. Friedman, J. L. Bentley, and R. A. Finkel, "An algorithm for finding best matches in logarithmic expected time," ACM Trans. Math. Softw. **3**, 209 (1977).
[50]A. Kempf, F. Flemming, and J. Janicka, "Investigation of lengthscales, scalar dissipation, and flame orientation in a piloted diffusion flame by LES," Proc. Combust. Inst. **30**, 557 (2005).
[51]S. B. Pope, "Ten questions concerning the large-eddy simulation of turbulent flows," New J. Phys. **6**, 35 (2004).
[52]P. E. Kloeden and E. Platen, *Numerical Solution of Stochastic Differential Equations, Applications of Mathematics, Stochastic Modelling and Applied Probability* (Springer, New York, 1995), Vol. 23.
[53]J. Xu and S. B. Pope, "PDF calculations of turbulent nonpremixed flames with local extinction," Combust. Flame **123**, 281 (2000).